PLOS Computational Biology

RESEARCH ARTICLE

The mechanism of dynamic steady states in lamellipodia

June Hyung Kim[1], **Taeyoon Kim**[1,2,3*]

1 Weldon School of Biomedical Engineering, Purdue University, West Lafayette, Indiana, United States of America, **2** EMBRIO Institute, Purdue University, West Lafayette, Indiana, United States of America, **3** Faculty of Science and Technology, Keio University, Kohoku Ward, Yokohama, Japan

* kimty@purdue.edu

OPEN ACCESS

Citation: Kim JH, Kim T (2025) The mechanism of dynamic steady states in lamellipodia. PLoS Comput Biol 21(10): e1013572. https://doi.org/10.1371/journal.pcbi.1013572

Editor: Mark Alber, University of California Riverside, UNITED STATES OF AMERICA

Received: December 30, 2024

Accepted: September 29, 2025

Published: October 7, 2025

Data availability statement: The code used for simulations can be downloaded from https://github.com/ktyman2/Lamellipodia.

Funding: Research reported in this publication was supported by the EMBRIO Institute, contract #2120200, the National Science Foundation Biology Integration Institute (to J.H.K and T.K.). The funder did not play any role in study design, data collection and

Abstract

Lamellipodia are quasi-two-dimensional actin projections formed on the leading edge of the cell, playing an important role in sensing surrounding mechanical environments by forming focal adhesions. A branched actin network in the lamellipodia exhibits a stable, yet dynamic steady state characterized by a retrograde flow, which is attributed to a balance between network assembly at the leading edge and disassembly at the rear. Although the molecular players and architecture of the lamellipodia have been investigated extensively during recent decades, it still remains elusive how the dynamic steady state with continuous retrograde flow is achieved and robustly maintained. Using an agent-based computational model, we probed how physical interactions between subcellular components in the lamellipodia mediate and sustain the dynamic steady state. We simulated the branched network found in the lamellipodia, consisting of F-actin, myosin motor, Arp2/3 complex, and actin cross-linking protein, on an elastic substrate. We reproduced a steady retrograde flow induced by myosin activity and balanced by the interplay between network assembly and disassembly, but hindered by resistances from adhesions formed on the underlying substrate. We found that F-actin severing is crucial for maintaining a continuous, uniform retrograde flow because it enhances the disassembly of actin bundle/arc formed due to network contraction at the rear. In addition, we demonstrated that different modes of dynamic steady states are possible, and that a network which failed to show the retrograde flow due to perturbations can be rescued by altering other factors. Our study provides insights into understanding how cells maintain the dynamic steady state of the lamellipodia in highly varying microenvironments.

Author summary

This study investigates the adaptive mechanisms that maintain the dynamic steady state conditions in the lamellipodia. Using simulations of the branched

analysis, decision to publish, or preparation of the manuscript.

Competing interests: The authors have declared that no competing interests exist.

actin network, we found that the balance between actin assembly and disassembly, and the competition between contractile forces and frictional forces govern the steady state conditions with continuous actin retrograde flow. We further found that the branched actin network can exhibit different modes of dynamic steady states, where perturbations preventing steady state can be compensated by adjusting other key parameters. This work advances our understanding of the complex interplay between subcellular components in lamellipodia, providing new insights into the adaptive robustness of the branched actin network in response to environmental changes.

Introduction

Cell migration plays a central role in various biological processes, including morphogenesis, immune responses, wound repair, and cancer metastasis [1–3]. One of the important steps for cell migration is cell protrusion, the outward extension of the plasma membrane. The cell protrusion allows cells to probe and sense surrounding environments by forming distinct actin architectures in response to different geometry of microenvironments. Two typical cell protrusions that emerge on cells migrating on a substrate are filopodia (finger-like) and lamellipodia (sheet-like). The lamellipodia comprise branched actin networks formed by Arp2/3 complex [4–8]. The Arp2/3 complex is activated primarily via Wiskott–Aldrich syndrome protein (WASP) family, such as the verprolin-like central acidic (VCA) domain of the WAVE regulatory complex [9–11]. After activation, Arp2/3 complex binds to the side of actin filaments (F-actins) to nucleate new filaments (branches) at the characteristic angle of ~70° [4,12–14]. Then, the branches elongate by polymerization with ATP-actin monomers. However, branch elongation does not last long since capping proteins quickly bind to elongating barbed ends to prevent further polymerization [15,16]. These elongating branches collectively push the cell membrane bearing tension outward, leading to the lamellipodial protrusion. Additionally, actin cross-linking proteins (ACPs), including α-actinin and filamin A, are known to help the branches push the membrane by physically interconnecting them [17,18].

The branched network is also continuously pulled toward the rear by contractile forces generated by myosin motors. The network is accumulated into bundles called actin arcs found at the interface between lamellipodia and lamella [19,20]. F-actins undergo ATP hydrolysis during movement toward the rear, becoming ADP-F-actin that is more prone to depolymerization and severing induced by cofilin which is also known as Actin Depolymerization Factor (ADF) [21–23]. As a result of F-actin disassembly, the actin arc is able to maintain a relatively consistent thickness rather than thickening over time from continuous accumulation of F-actins [20]. Actin monomers generated from F-actin disassembly bind to profilin to avoid de novo (spontaneous) nucleation and switch to ATP-G-actin more rapidly [24–26]. These profilin-bound actin monomers are further transported to the leading edge to be used for the elongation of new branches. Additionally, myosin II contributes not only as a contractile force

generator but also as a disassembly promotor at the cell rear [27]. Coordinated, balanced activities of these proteins result in a dynamic steady state characterized by the actin retrograde flow from the leading edge to the rear. F-actins in the lamellipodia keep forming focal adhesions (FAs) on an underlying substrate via integrin proteins, which enables cells to exert traction forces required for mechanosensing and cell migration and to impede the actin retrograde flow [28–31].

The dynamic steady state of branched actin networks in the lamellipodia has been well-characterized in live cells [5,6,16,17,20,24,25,28,31]. Systems with cell extract encapsulated in water-in-oil droplets showed persistent contractile flows [32], but the exact contribution of each protein in the cell extract to mediating the flow and maintaining its dynamic steady state is still unclear. Reconstituted systems composed solely of purified cytoskeletal proteins have replicated part of the dynamic steady state. For example, a recent study demonstrated a treadmilling steady state (i.e., balance between assembly and disassembly) achieved by a minimal reconstituted actomyosin cortex built with purified proteins on a lipid bilayer [33]. This study discussed the origin of network thickness robustness, the role of actin treadmilling in the steady state, the non-linear dependence of actin treadmilling speed on the concentration of disassembly proteins, and the effect of myosin motors on actin turnover. While this system showed a polarized network and a treadmilling flow, it did not account for the biased spatial distribution of myosin II and interactions between the actin network and an extracellular environment through FAs. Despite these previous efforts, the exact combination and concentrations of proteins required to reproduce the lamellipodial dynamic steady state remain unclear. In addition, this dynamic steady state is surprisingly robust. Lamellipodia constantly adapt to changes in environmental cues (e.g., stiffness and adhesion conditions) by varying their dynamic steady state [34,35]. Despite experimental observations, how the lamellipodia show such high adaptability to environments remains to be explained.

Mathematical and computational models can help illuminate the mechanisms of the dynamic steady state exhibited by branched actin networks in the lamellipodia and their adaptability by overcoming intrinsic limitations of experiments. Mathematical models based on partial differential equations described branched actin networks as a quasi-2D viscous flow [36] or their local actin concentration in 1D [37,38]. Although these mathematical models showed how actin turnover, protrusive forces, motor activity, FA dynamics, and interactions with substrates regulate the retrograde flow, detailed mechanisms cannot be uncovered by such drastically simplified models. Several agent-based computational models have been employed to simulate the detailed structure of branched actin networks. However, most of them focused only on protrusion driven by actin polymerization, not on the retrograde flow [39–43]. A recent agent-based model showed how the retrograde flow speed and morphology of branched actin networks are affected by physical interactions with a single matured FA site [44]. However, the flow was induced by applying external forces rather than interactions with myosin motors, and network disassembly was not described in a realistic manner. We recently developed a filament-level model to reproduce the actin retrograde flow induced by myosin activity against resistances from many nascent FA sites formed on an underlying substrate, but the flow took place only once without a steady state due to the absence of actin dynamics [16]. Despite these previous efforts, there has not been any model capable of reproducing the dynamic steady state of lamellipodia without drastic simplification of cytoskeletal elements and structures.

In this study, we developed a rigorous model for the lamellipodia with detailed descriptions of physical interactions between key molecular players identified in experiments. Our model was able to reproduce the steady-state retrograde flow emerging from a balance between network assembly at the leading edge, network disassembly and motor activity at the rear, and nascent FAs forming between the network and the underlying substrate. However, when this balance was perturbed by a change in one of factors, the dynamic steady state disappeared. We further demonstrated how the dynamic steady state can be achieved again to adapt to the perturbation. Our study provides insights into understanding the resilient maintenance and recovery of the dynamic steady state observed in the lamellipodia.

Results

An agent-based model is developed to simulate dynamic interactions between key molecular players in the lamellipodia, including F-actin, molecular motor, Arp2/3 complex, and ACP (Fig 1A). In our model, F-actin is simulated as serially

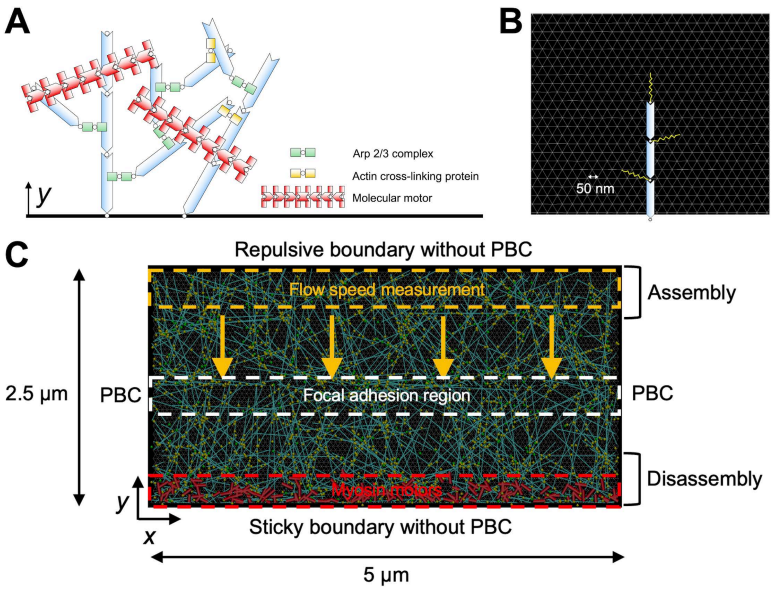

Fig 1. The lamellipodia model. (A) A branched network is created by self-assembly and interactions of F-actin (cyan), Arp2/3 complex (green), ACP (yellow), and motor (red), all of which are simplified via cylindrical segments. **(B)** An underlying substrate is simplified into a triangulated mesh with the chain length of 50 nm (gray). The endpoints of actin segments can transiently form an elastic link (yellow) to the substrate. **(C)** Description of different regions for dynamic events in the computational domain (5 μm × 2.5 μm). Actin polymerization occurs only in the assembly region (y = 2.125 - 2.5 μm), whereas actin depolymerization takes place only in the disassembly region (y = 0 - 0.375 μm). Motors are initially located near the -y boundary (y = 0 - 0.1875 μm). The links between the substrate and the network can form only in the focal adhesion region (y = 0.325 - 0.675 μm). We use F-actins located near the +y boundary for the calculation of retrograde flow speed. The periodic boundary condition is applied in the x direction, whereas repulsive and sticky boundary conditions are applied to the +y and -y boundaries, respectively.

https://doi.org/10.1371/journal.pcbi.1013572.g001

connected cylindrical segments with polarity defined by the barbed and pointed ends. Arp2/3 and ACP consist of two segments connected in series, whereas motors are simplified into a backbone connected to 8 motor arms. Each of the motor arms kinetically represents 4 myosin heads. F-actin can undergo de novo nucleation, polymerization, depolymerization, and angle-dependent severing. Arp2/3 binds to the side of existing F-actin to nucleate a new filament at the characteristic branching angle of 70°. ACP connects pairs of F-actins to form functional cross-linking points. Each motor arm binds to F-actin and walks toward the barbed end of F-actin, and it also unbinds from F-actin in a force-dependent manner. An underlying substrate is coarse-grained into a triangulated mesh with nodes whose z positions are fixed at z = 0 (Fig 1B). Nascent FAs are mimicked by transiently forming elastic links between the endpoints of actin segments and the substrate nodes (Fig 1B). The displacements of substrate nodes and all the segments constituting F-actin, Arp2/3, ACP, and motor are determined by the Langevin equation based on Brownian dynamics. To mimic the geometry of the lamellipodia, a relatively thin 3D domain (5 × 2.5 × 0.1 μm) is employed (Fig 1C). The +y boundary and -y boundary are considered the leading edge and the interface between lamellipodia and lamella, respectively. At the beginning of simulation, a branched actin network is assembled from filament seeds. ~ 90% of actin is used for assembling the network. During network assembly, dynamic behaviors of F-actin, Arp2/3, ACP, motor, and FA described earlier take place except motor walking. Motors are located only near the -y boundary, and FAs are allowed to form within a specific region, unlike the other elements (Fig 1C). After network assembly, motors start walking along F-actins, leading to a retrograde flow. In addition, F-actins are polymerized from the barbed ends only near the leading edge and depolymerized from the pointed ends only near the -y boundary (Fig 1C). F-actins can also be severed anywhere at a rate proportional to a local bending angle. Even without any spatial constraint, F-actin severing predominantly takes place in the region where the network is compacted into a

bundle (mimicking the actin arc) due to the motor activity [27,45]. Free actin segments generated from F-actin disassembly and severing can be recycled for network assembly occurring near the leading edge, allowing for a continuous actin retrograde flow. All of these dynamic behaviors and interactions can allow the branched actin network to reach a dynamic steady state under specific conditions as shown later.

Using our model, we explored a wide parametric space to find conditions for the continuous retrograde flow in the dynamic steady state. We identified a condition where the dynamic steady state was maintained over 200 s. Under this reference condition, network morphology was similar regardless of time points (Fig 2A and S1 Movie). The number of FAs forming on the underlying substrate and the total force acting on the underlying substrate did not vary significantly over time after 100 s (Fig 2B-D). The retrograde flow speed spatiotemporally remained relatively steady after 100 s (Fig 2E-F). Actin density was relatively homogeneous, but a slightly denser structure periodically formed near the leading edge and then moved toward the rear (Fig 2G). As we will show later, this is caused by a somewhat low flow rate. At 50–100 s, the flow speed was lower because local actin concentration in the motor-activated region was lower in the time range (Fig 2E-G); it took more time for motors to bind to F-actins and generate contractile forces for recovering the flow speed. In the following results, we varied the values of key parameters to understand how the dynamic steady state is altered and maintained.

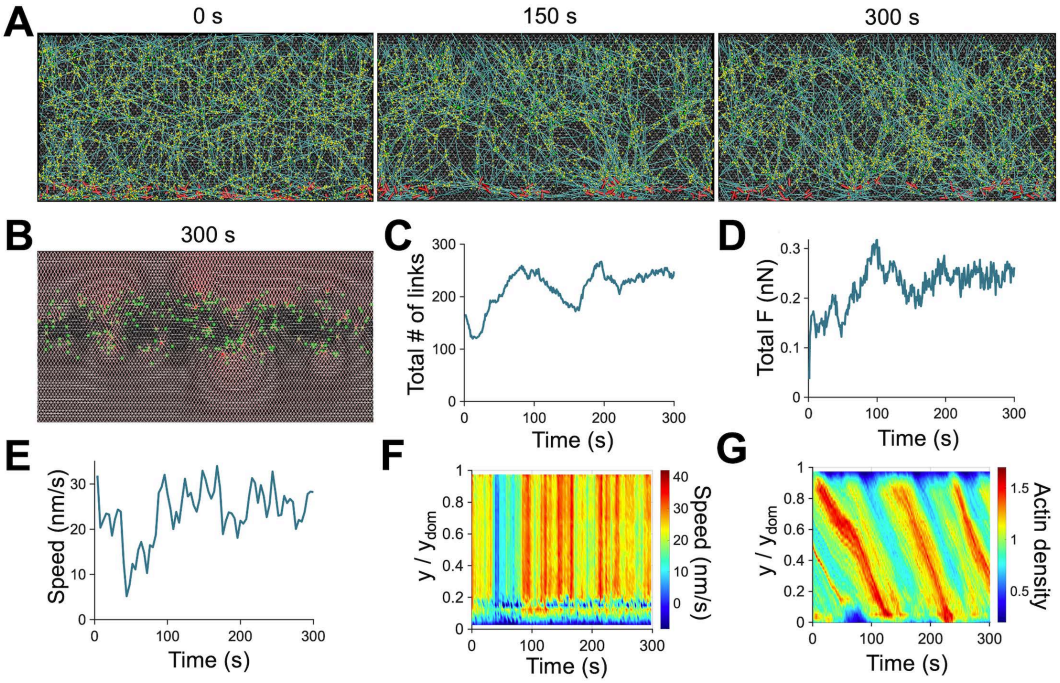

Fig 2. The dynamic steady state of the branched network under the reference condition. (A) Snapshots of networks taken at 0 s, 150 s, and 300 s. The network was homogeneous and maintained continuity regardless of time points. **(B)** Snapshot showing links (green circles) formed in the focal adhesion region (y = 0.81 - 1.69 μm) and forces acting on the underlying substrate via color scaling (red: high force, white: low force) taken at 300 s. **(C)** Time evolution of the number of the links formed between the substrate and the network. **(D)** The total substrate force exerted by the network via the links as a function of time. **(E)** Time evolution of retrograde flow speed. **(F)** Kymograph of flow speed as a function of y position and time. Quantities shown in (C-F) change more at $t < 100$ s but exhibit smaller fluctuations around average values after 100 s. **(G)** Kymograph of actin density as a function of y position and time. Low actin density at $y < 0.1$ μm between 50 s and 100 s is indicative of the lack of overlap between F-actins and motors. Thus, it took more time for motors to bind and walk along F-actins to recover the retrograde flow, which explains large fluctuations shown in **(C-F)**. Under this reference condition, key parameter values are $k_{+,A} = 12\ \mu M^{-1}s^{-1}$, $R_{ACP} = 0.04$, $R_{Arp2/3} = 0.01$, $k_{-,A} = 6\ s^{-1}$, $k_{0,sev} = 10^{-45}\ s^{-1}$, $\lambda_{sev} = 1.0\ deg^{-1}$, $R_M = 0.004$, $k_{20} = 17\ s^{-1}$, and $A_{FA} = 0.35$.

https://doi.org/10.1371/journal.pcbi.1013572.g002

Proper assembly and connectivity of networks are required for maintaining the dynamic steady state

We first investigated the effects of a variation in parameters governing network assembly on the dynamic steady state. We found that actin polymerization occurring near the leading edge should be fast enough for maintaining a continuous branched network structure. When F-actins were polymerized too slow due to low actin polymerization rate constant ($k_{+,A}$ = 0.4 $\mu M^{-1}s^{-1}$), the contracting network lost connection to newly assembled F-actins near the leading edge, resulting in the loss of a steady state (S2A, S2F, and S2G Fig). Slow actin polymerization further led to a pronounced oscillation in actin density (S2C and S2E Fig). With $k_{+,A}$ higher than 1 $\mu M^{-1}s^{-1}$, the continuity of the network structure was sustained in the flow direction, and the oscillation did not appear. The retrograde flow speed was also relatively steady only when the network showed continuity in the flow direction (S2F and S2G Fig). A further increase in $k_{+,A}$ did not make a difference in network behaviors because it was assumed in the model that the concentration of free actin monomers is enforced to stay above 10% of the total actin concentration (S2B and S2D-G Fig). In other words, the availability of actin monomers provided from depolymerization and severing at the rear becomes a limiting factor for actin turnover if actin polymerization is sufficiently fast.

The influence of a variation in Arp2/3 density ($R_{Arp2/3}$) was also tested because Arp2/3 plays a critical role in network assembly by forming new branches from existing F-actins near the leading edge. The lack of Arp2/3 ($R_{Arp2/3}$ = 0.006) caused a decrease in the flow speed since the formation of new branches was unable to keep up with the network disassembly occurring at the rear near the -y boundary (S3A, S3F, and S3G Fig). This led to the accumulation of F-actin and significant oscillation in actin density (S3C and S3E Fig). High Arp2/3 density ($R_{Arp2/3}$ = 0.016) resulted in the formation of more branches on a fraction of vertically growing structures, so the network became more heterogeneous in the x direction with lower connectivity (S3B Fig). Despite high heterogeneity in the x direction, $R_{Arp2/3}$ above threshold level ($R_{Arp2/3} \geq 0.008$) resulted in a continuous retrograde flow, and there was no significant effect of a further increase in $R_{Arp2/3}$ on flow speed because network disassembly is the limiting factor as described earlier (S3D-G Fig).

In our model, branches always form toward the leading edge. Thus, one filament seed created on the -y boundary grows as a relatively narrow (in the x direction) branched network up to the leading edge. Although all F-actins within this structure have superior connectivity via permanently bound Arp2/3, connection between structures originating from different filament seeds does not exist. ACPs connect pairs of branches to enhance network connectivity in the x direction. To understand the importance of network connectivity in the direction perpendicular to the flow, we varied ACP density (R_{ACP}). With sufficiently high ACP density ($R_{ACP} \geq 0.02$), the network could contract as a single entity and maintain a steady retrograde flow (S4B and S4D-G Fig). With low ACP density ($R_{ACP} < 0.02$), forces generated by motors were not uniformly transmitted through an entire network due to lack of network connectivity (S4A Fig). Thus, the network could not contract as a whole and was stalled due to frictional forces from FAs (S4C and S4E-G Fig). In sum, the sufficiently fast assembly of a well-connected network is required for the dynamic steady state with a continuous retrograde flow and uniform network contraction.

Network disassembly via depolymerization and severing is critical for maintaining the dynamic steady state

Considering the importance of actin disassembly as the limiting factor for actin turnover, we next probed how network morphology and retrograde flow are regulated by the depolymerization and severing of F-actins. First, the depolymerization rate was varied by changing the value of actin depolymerization rate ($k_{-,A}$). We found that the dynamic steady state with physiologically relevant retrograde flow speed emerged when the actin depolymerization was neither too fast nor too slow. The absence of actin disassembly ($k_{-,A} = 0\,s^{-1}$) resulted in the accumulation of F-actins towards the -y boundary, corresponding to one-time, irreversible contraction of the branched network (Fig 3A and 3C), which we showed in our recent study [16]. The flow speed decayed over time as F-actin accumulated towards the -y boundary (Figs 3F and S5A). By contrast, cases with very fast depolymerization ($k_{-,A} \geq 8\,s^{-1}$) led to the rapid depolymerization of F-actins prior to

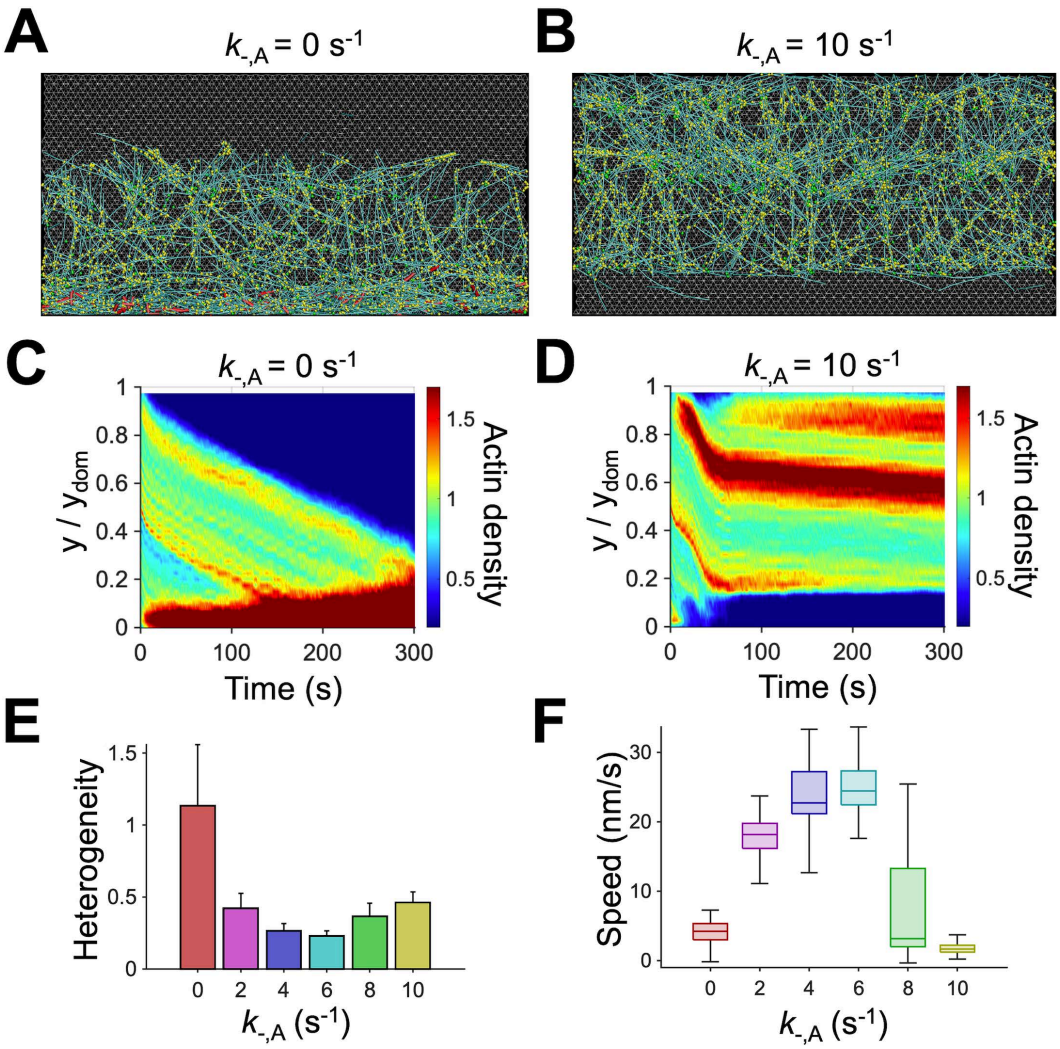

Fig 3. Intermediate actin depolymerization rate led to a continuous flow with uniform network morphology. (A, B) Snapshots of branched networks taken at ~150 s with a lower (0 s^{-1}) or higher (10 s^{-1}) value for actin depolymerization rate ($k_{-,A}$) relative to that of the reference condition, 6 s^{-1}. Network contraction without actin depolymerization led to loss of connection between the network and the leading edge, whereas too fast actin depolymerization resulted in loss of connection between the network and the motors. **(C, D)** Kymographs of actin density as a function of y position and time with different $k_{-,A}$. **(E)** Heterogeneity of the network quantified as a coefficient of variation in actin density in the y direction. A lower value is indicative of a more homogeneous network. The network without actin depolymerization ($k_{-,A}$ = 0 s^{-1}) showed very high heterogeneity which is attributed to the severe network accumulation shown in **(A)**. **(F)** Retrograde flow speed for different values of $k_{-,A}$. With intermediate values of $k_{-,A}$, the network was more homogenous, and the flow speed was comparable with experimental observations.

https://doi.org/10.1371/journal.pcbi.1013572.g003

motor-mediated network contraction, causing disconnection between the network and the motors (Fig 3B and 3D). As a result, the retrograde flow disappeared after 100 s (Figs 3F and S5A). With intermediate depolymerization rates ($k_{-,A}$ = 4–6 s^{-1}), the flow speed was high and steady, and the network showed relatively homogeneous actin distribution similar to the reference case (Fig 3E and 3F).

It was shown experimentally that F-actin could be severed at an angle-dependent rate during thermal fluctuation [46]. In our previous study, we have shown that angle-dependent F-actin severing can drive the reversible (i.e., pulsatile) contraction of actomyosin networks by enhancing the disassembly of aggregating networks [47]. In our model, it is assumed that

F-actin severing occurs in an angle-dependent manner in an entire domain. As before, the severing rate is determined by two parameters: actin severing rate constant ($k_{0,sev}$) and angle sensitivity (λ_{sev}) (Eq. S9). We probed the effects of a variation in $k_{0,sev}$ and λ_{sev} on the dynamic steady state. The dynamic steady state was maintained well with steady flow speed and homogeneous network morphology only when $k_{0,sev}$ was at intermediate level, $k_{0,sev} = 10^{-55}$–10^{-45} (Figs 4E, 4F and S5B). The absence of severing ($k_{0,sev} = 0$) led to the stalling of network contraction at early times (Fig 4A and 4C). As F-actins in the motor region were disassembled, the network eventually lost connection to the motors. As a result, the branched network failed to reach a steady state and became noticeably heterogenous with a high variation in F-actin density in the

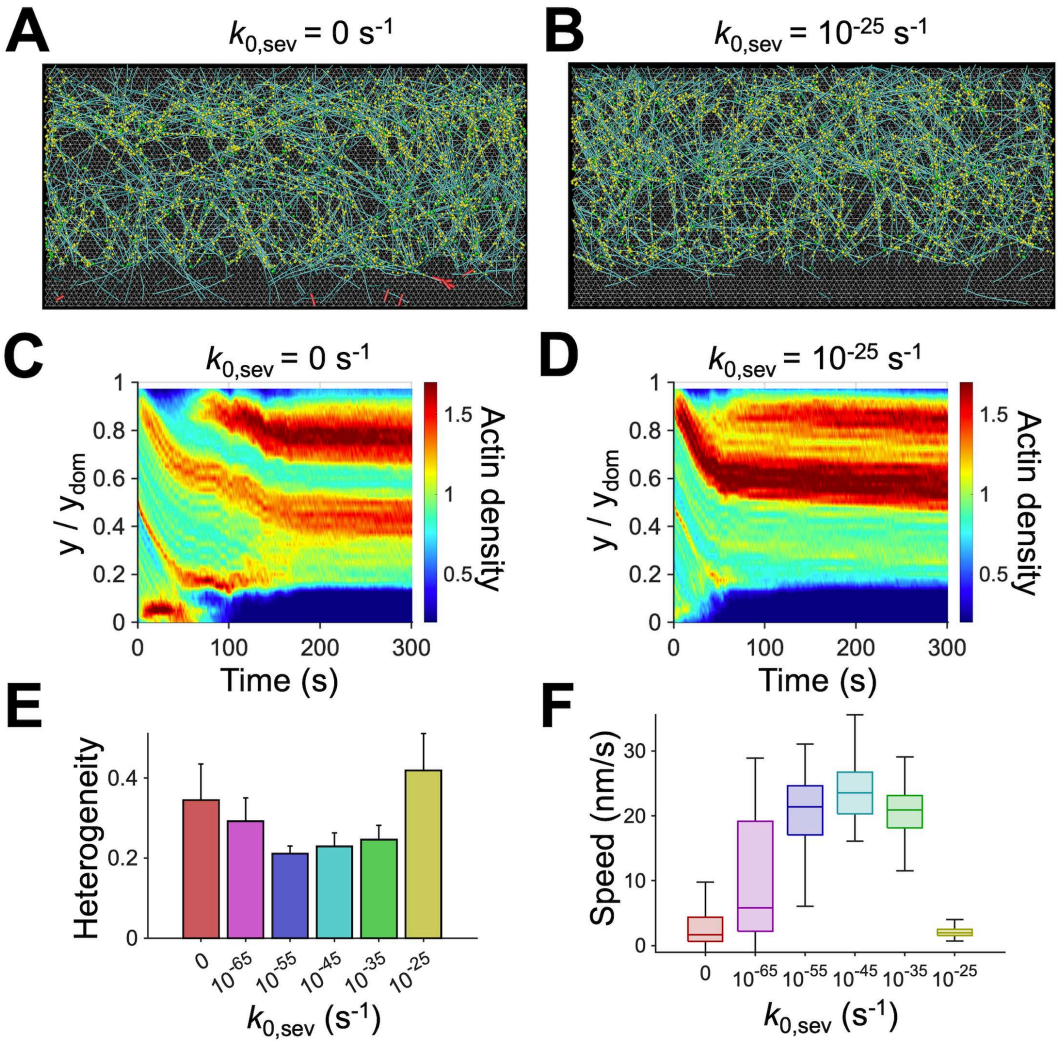

Fig 4. Intermediate F-actin severing activity is necessary to maintain a dynamic steady state. (A, B) Snapshots of the branched networks taken at ~150 s with a lower (0 s^{-1}) or higher (10^{-25} s^{-1}) value of severing rate constant ($k_{0,sev}$) relative to that of the reference condition, 10^{-45} s^{-1}. In the absence of severing, a bundle structure was formed by the initial accumulation of F-actins. Due to the delayed disassembly of the bundle, motors remained trapped within the bundle until ~60 s and could not induce further network contraction. Once the bundle was finally disassembled by depolymerization, motors were unable to find F-actins to bind, leading to disconnection between the network and the motors. With fast severing activity, the filaments were immediately disassembled before motors could induce contraction, and the network eventually lost connection to the motors. **(C, D)** Kymographs of actin density as a function of y position and time with different $k_{0,sev}$. **(E)** Heterogeneity of the network quantified as a coefficient of variation in actin density in the y direction. **(F)** Retrograde flow speed for different $k_{0,sev}$. With intermediate values of $k_{0,sev}$, network was more homogeneous, and the flow was faster with smaller fluctuations.

https://doi.org/10.1371/journal.pcbi.1013572.g004

y direction (Fig 4C, 4E, and 4F). Highly branched, cross-linked networks are hard to contract into bundles due to their high compressive resistance; the length of buckling units in these networks is very short, so large contractile forces are necessary to buckle them for network contraction. The angle-dependent severing can make the network contraction easier. Thus, without severing, the network contraction was stalled. Frequent F-actin severing ($k_{0,sev} = 10^{-25}$) induced rapid fragmentation of F-actins in the motor region, where F-actins experience an increase in their bending angles due to buckling induced by network contraction (Fig 4B, 4D, and 4F). This led to rapid loss of connection between the network and the motors. Thus, the flow speed and the actin density showed biphasic dependence on $k_{0,sev}$.

A variation in λ_{sev} led to similar results (S6 Fig). With higher λ_{sev}, the severing rate becomes more sensitive to a change in local bending angles on F-actins induced by buckling. When λ_{sev} was very high ($\lambda_{sev} = 2.5\ deg^{-1}$), severing occurred even by a small increase in the bending angles, and excessively frequent severing led to results similar to those with high $k_{0,sev}$ (S6B and S6D-G Fig). When λ_{sev} was small ($\lambda_{sev} = 0.5\ deg^{-1}$), F-actin severing hardly took place, resulting in the stalling of network contraction and the loss of connection between the network and the motors similar to cases with $k_{0,sev} = 0$ (S6A, S6C, and S6E-G Fig). In sum, network disassembly mediated by steady actin depolymerization and angle-dependent severing should take place at moderate rates for maintaining the dynamic steady state.

A minimal number of motors are required for a continuous actin retrograde flow against friction from FAs

In this model, network contraction induced by motors located near the -y boundary is a main driving factor for the retrograde flow. We probed the impact of a variation in motor density (R_M). An insufficient number of motors ($R_M \leq 0.003$) resulted in a negligible retrograde flow and minimal network contraction because forces generated by the motors were not large enough to overcome friction exerted by FAs (Figs 5F, 5G and S5C). Since network disassembly continuously occurred near the -y boundary, the stationary network eventually lost connection to motors (Fig 5A, 5C, and 5E). When R_M was increased from 0.003 to 0.005, the flow speed was abruptly increased with noticeable network contraction, implying that motor-generated forces became larger than the frictional forces exerted by FAs (Figs 5F, 5G and S5C). A further increase in the number of motors ($R_M \geq 0.005$) still led to a steady flow, but F-actins began to accumulate towards the -y boundary because the network contraction was faster than network disassembly occurring near the -y boundary, which is reminiscent of the formation of actin arcs (Fig 5B, 5D, 5E, and 5F). We measured a total force transmitted from the network to the underlying substrate by summing forces acting on individual FAs. The total force was proportional to R_M up to $R_M = 0.005$ and became independent of R_M at $R_M > 0.005$ because maximum forces that FAs can transmit are limited by the force-dependent unbinding of links forming FAs (Fig 5G). When R_M was increased beyond 0.005, the frictional forces were relatively constant, but forces generated by motors increased, resulting in higher flow speed.

In addition to motor density, we probed the effect of the ATP-dependent unbinding rate (k_{20}) of myosin heads which is one of the mechanochemical rates used in the parallel cluster model [48,49]. The walking and unbinding rates of motors in our model tend to be proportional to k_{20}. With low transition rate ($k_{20} = 2\ s^{-1}$), the network failed to reach a steady state because the motors walk along F-actins more slowly, resulting in lower flow speed (S7A, S7C, S7E-H Fig). Beyond threshold walking speed ($k_{20} \geq 6\ s^{-1}$), the network reached steady state, and the network heterogeneity noticeably decreased (S7B and S7D-H Fig). With $k_{20} = 17\ s^{-1}$ used for physiologically relevant walking speed of non-muscle myosin II (120 nm/s) [50,51] in the reference condition, the network showed stable flow speed and relatively homogenous morphology (S7E-H Fig).

In sum, a sufficient number of motors are necessary to overcome resistances from FAs and induce a steady retrograde flow, and with more, faster motors, the flow becomes faster, leading to F-actin accumulation into a bundle.

Large frictional forces from FAs can frustrate the retrograde flow

In our model, FAs can be formed only in a specific region which spans across the entire domain in the x direction but occupies only a fraction of the domain in the y direction (Fig 1C). We varied the size of the FA region by altering its fraction relative to the entire domain size (A_{FA}) to investigate the effects of frictional forces from FAs on the dynamic steady state. Without FA region

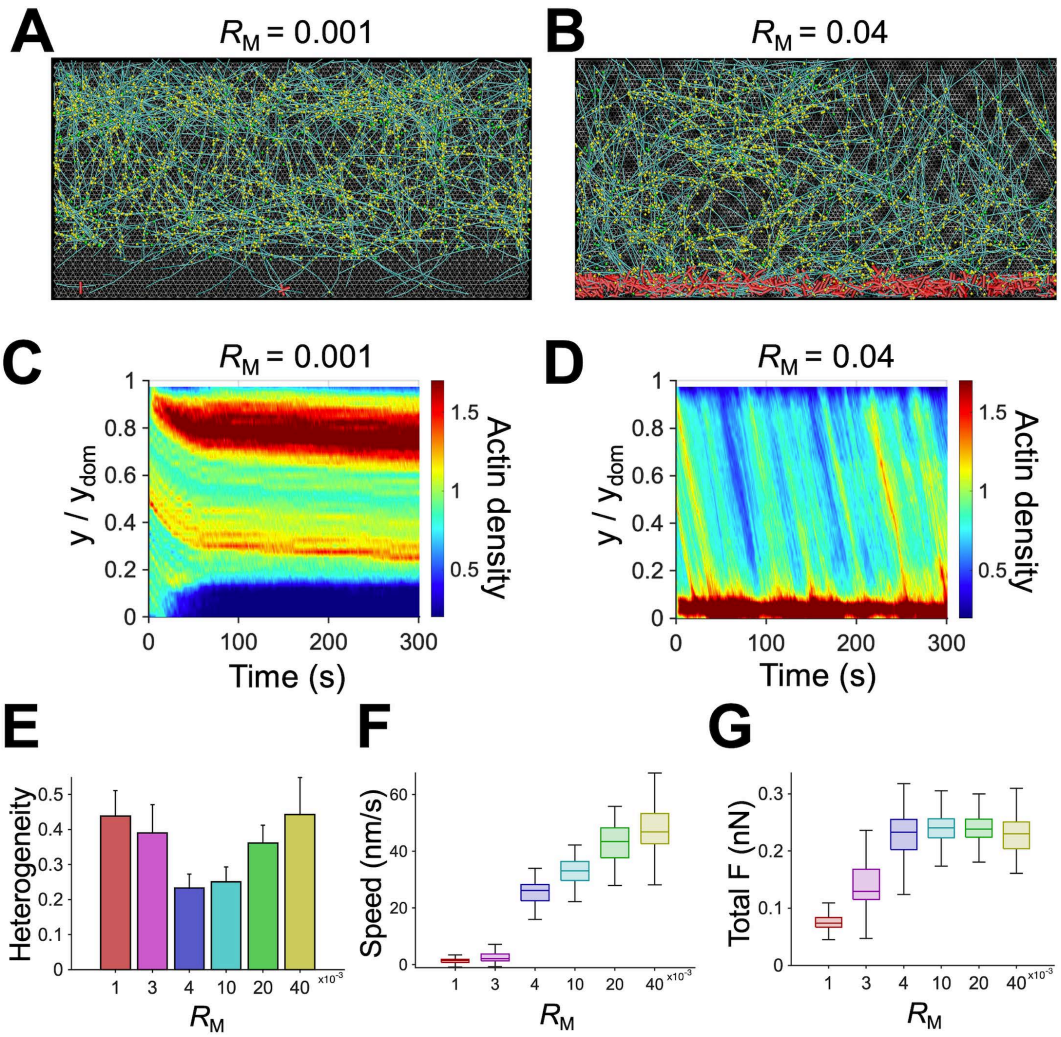

Fig 5. An increase in motor density makes the retrograde flow faster by enhancing contractile forces. (A, B) Snapshots of the branched network taken at ~150 s with a lower (0.001) or higher (0.04) value of motor density (R_M) relative to that of the reference condition, 0.004. **(C, D)** Kymographs of actin density as a function of y position and time with different values of R_M. The case with insufficient motors did not show a noticeable flow because it could not overcome frictional forces from FAs. As R_M increased, more F-actins were accumulated as a bundle near the -y boundary. **(E)** Heterogeneity of the network quantified as a coefficient of variation in actin density in the y direction. The network was most homogeneous with intermediate values of R_M. **(F)** Actin retrograde flow speed depending on R_M. With higher R_M, the flow tended to be faster. **(G)** Total force acting on the entire substrate via elastic links with different R_M. The total force showed a clear plateau at high R_M.

https://doi.org/10.1371/journal.pcbi.1013572.g005

(A_{FA} = 0), the retrograde flow speed was the highest, and the network was slightly accumulated near the -y boundary (Figs 6A, 6C, 6E-G and S5D), similar to observations in the case with high R_M. Consistent with experimental results [52,53], larger FA region resulted in a slower retrograde flow (Figs 6B, 6D-G and S5D). With the largest FA region that we tested (A_{FA} = 0.5), the network was stalled at the FA region and eventually disconnected from motors, resulting in higher heterogeneity and lower flow speed. This is similar to observations made in the case with very low R_M. A total force transmitted between the network and the underlying substrate increased in proportion to A_{FA} (Fig 6G), with a slight decrease for the case with A_{FA} = 0.5 which failed to reach a steady state. When the total force was close to maximum forces generated by motors (A_{FA} > 0.4), the retrograde flow was frustrated and disappeared after ~100 s (Figs 6F, 6G and S5D). Overall, an increase in A_{FA} led to results similar to those resulting

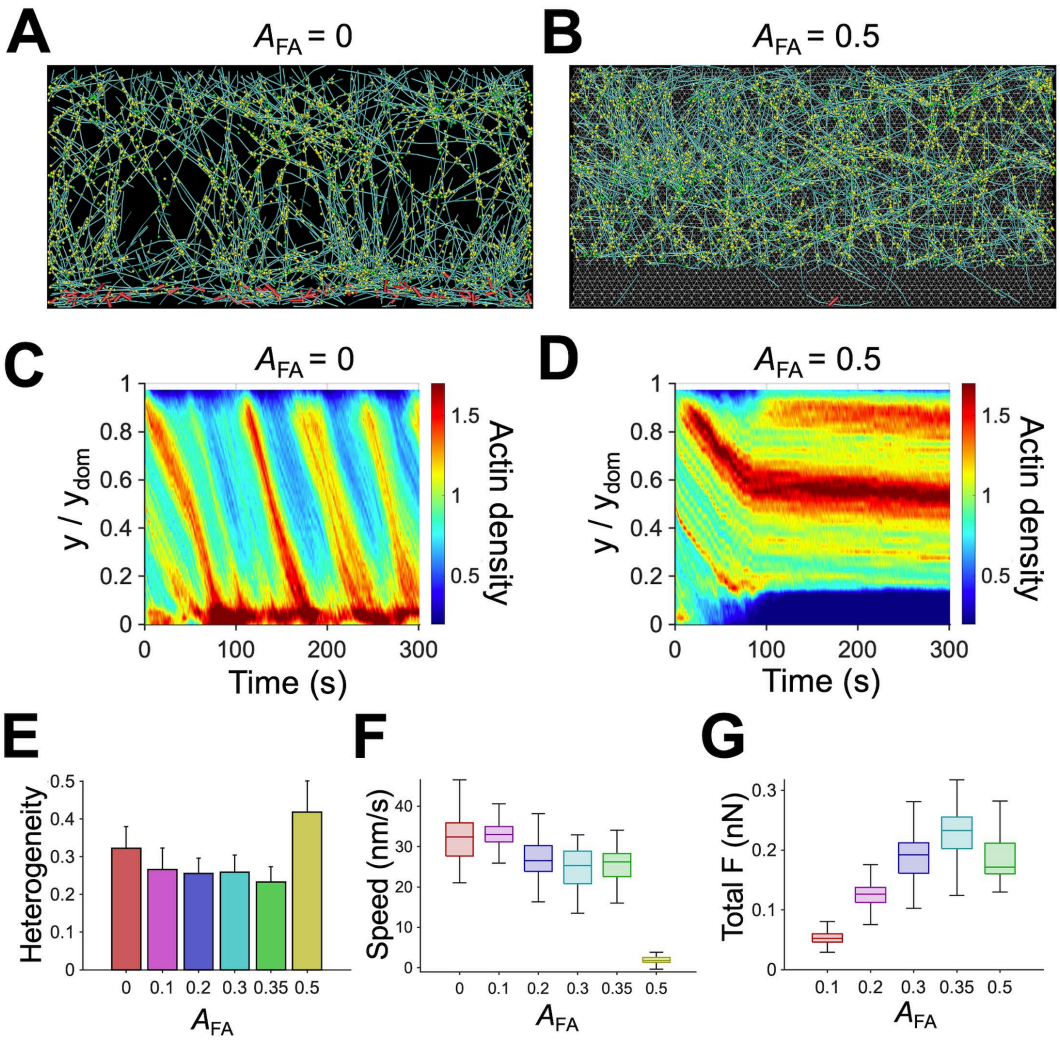

Fig 6. Focal adhesions (FAs) hinder the actin retrograde flow by exerting frictional forces. (A, B) Snapshots of the branched network taken at ~150 s with smaller (0) or larger (0.5) size of the FA region (A_{FA}) relative to that of the reference condition, 0.35. **(C, D)** Kymographs of actin concentration depending on time and y position with A_{FA}. Without the FA region, the accumulation of F-actins into a bundle was noticeable, whereas large FA region led to discontinuity between the network and the motors. **(E)** Heterogeneity of the network quantified as a coefficient of variation in actin density in the y direction. **(F)** Actin retrograde flow speed depending on A_{FA}. The flow speed tended to be smaller with larger FA region due to higher frictional forces. **(G)** Total force acting on the substrate by the network with different A_{FA}. At $A_{FA} \leq 0.35$, the total substrate force was proportional to A_{FA} due to the formation of more links, but the case with $A_{FA} = 0.5$ showed a lower total force because of the discontinuity between the network and the motors occurring at later times.

https://doi.org/10.1371/journal.pcbi.1013572.g006

from a decrease in R_M because the retrograde flow originates from a competition between force generation from motors and frictional resistances from FAs. If contractile forces are greater than frictional forces, a steady flow emerges, and network connectivity is maintained well. If not, the flow does not appear, and the network can undergo structural discontinuity.

Various dynamic steady states can exist

We have presented results from simulations with a variation in only one parameter relative to the reference case to demonstrate under what condition the dynamic steady state is maintained or disrupted. Our results suggest that the balance between network assembly and disassembly and the competition between contractile forces and frictional forces

lead to the dynamic steady state characterized by the continuous retrograde flow. It is likely that there can be various dynamic steady states with different retrograde flow speed as long as minimum conditions for the dynamic steady state can be satisfied. Indeed, it has been experimentally observed that the lamellipodia exhibited different states and switched between them to adapt to varying environments. For example, a branched actin network underwent significant structural changes in response to mechanical loads transmitted from the extracellular environment [54,55]. We explored the possibility of different modes of dynamics steady states. Based on the observation that a decrease in R_M has opposite effects on flow speed and network contraction to those of a decrease in A_{FA} (Figs 5 and 6), we first investigated whether a decrease in A_{FA} can rescue the case that failed to reach a steady state due to very low $R_M = 0.0015$. When the FA region was reduced from $A_{FA} = 0.175$ to $A_{FA} = 0$, a steady and fast retrograde flow emerged because contractile forces generated by motors could be used solely for network contraction without a competition against frictional forces exerted by FAs (Fig 7A and 7C). Alternatively, the case that failed to show the actin retrograde flow due to high A_{FA} could be rescued by increasing R_M from 0.0015 to 0.004 (Fig 7A and 7C).

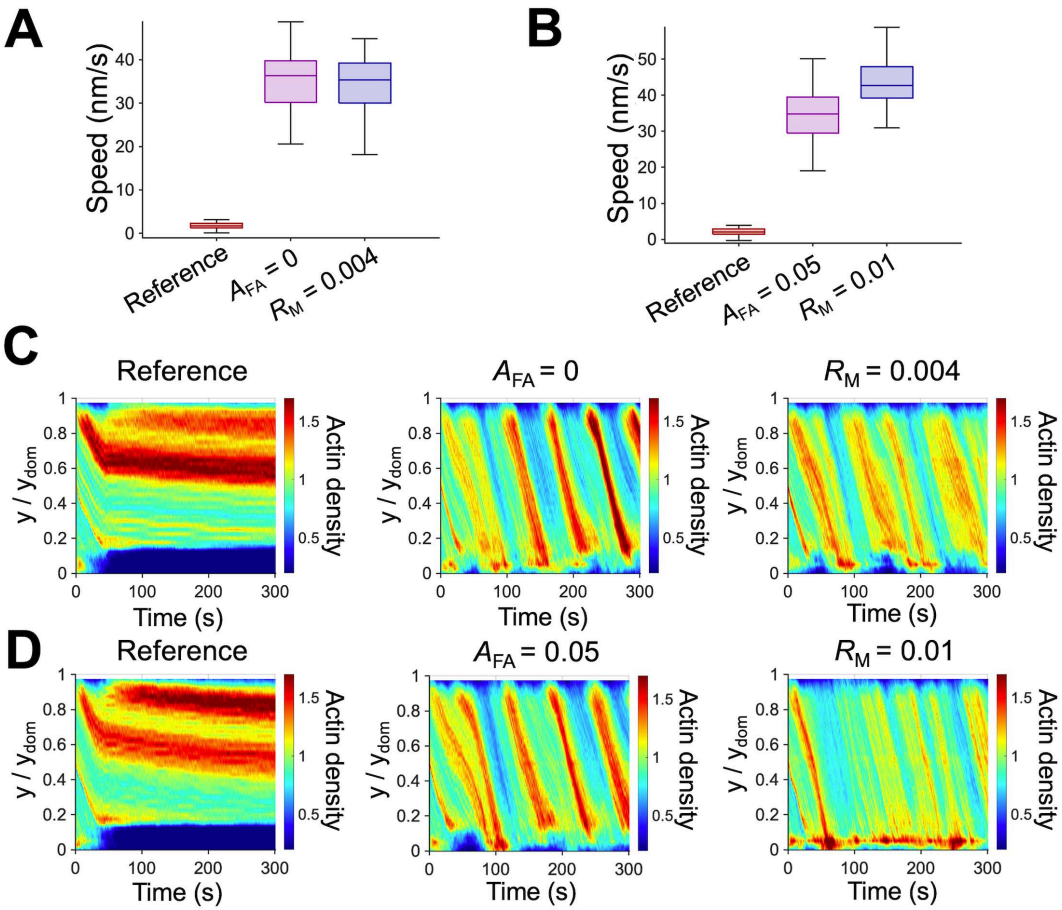

Fig 7. Different modes of dynamic steady states exist. (A) Two ways to rescue the case showing a negligible flow with $R_M = 0.0015$, $A_{FA} = 0.175$, and $k_{-A} = 6\,s^{-1}$. Since contractile forces were insufficient to overcome the frictional forces in this case, it was able to be rescued by either increasing R_M to 0.004 or reducing A_{FA} to 0. **(B)** Rescuing a case exhibiting a minimal flow with $R_M = 0.004$, $A_{FA} = 0.15$, and $k_{-A} = 10\,s^{-1}$. Since actin depolymerization was too fast compared to flow speed, this case was able to be rescued by enhancing flow speed, either by increasing R_M to 0.01 or decreasing A_{FA} to 0.05. **(C, D)** Kymographs of actin density as a function of y position and time for cases shown in **(A)** and **(B)**, respectively.

https://doi.org/10.1371/journal.pcbi.1013572.g007

We previously showed that fast depolymerization ($k_{-,A} = 10\,s^{-1}$) resulted in the loss of network connectivity near the -y boundary due to excessively fast network disassembly, preventing motors from binding and properly walking along F-actins. We next tested whether increasing the flow speed to match the fast depolymerization rate can rescue the case. We found that a steady flow was restored with either lower A_{FA} or higher R_M (Fig 7B and 7D), showing how the competition between contractile and frictional forces is related to the balance between network assembly and disassembly. A notable difference is that the restored flow speed was considerably faster than that observed in the reference case. A decrease in the frictional forces or an increase in contractile forces caused the network to flow more readily towards the -y boundary, which supplied enough F-actins for motors to bind and walk along before former F-actins were completely disassembled. All of these results suggest that different types of dynamic steady states exist and a switch between these states is possible by adjusting the appropriate parameters.

Discussion

Lamellipodia, sheet-like cell protrusions, have been extensively studied during recent decades. Although the underlying molecular players and working principles for lamellipodia have been identified, it remains unclear how the dynamic steady state is maintained despite environmental changes. In this study, we simulated the branched actin network in the lamellipodia to define the mechanism of adaptive maintenance of the actin retrograde flow. We succeeded in reproducing a steady-state retrograde flow driven by actin dynamics and motor activity against FAs (Fig 2). Through parametric studies, we showed the importance of a balance between network assembly near the leading edge and network disassembly at the rear end of the lamellipodia.

First, we found that sufficiently fast actin polymerization and high Arp2/3 density enabled the network to maintain a continuous retrograde flow by timely creating new branches near the leading edge (S2 and S3 Figs). When branch formation was delayed due to either slow actin polymerization or insufficient Arp2/3 complexes, network assembly was unable to keep up with network disassembly, resulting in network discontinuity. We also showed that a large number of ACPs could lead to the uniform contraction of an entire network toward the rear as a single entity by enhancing network connectivity (S4 Fig). This is consistent with our previous study which showed that many cross-linking points between F-actins were required for global network contraction into a single cluster [56]. In the lamellipodia, new branches are formed toward the leading edge with the characteristic angle of 70º, so it is hard to expect that the network has percolation in a direction perpendicular to the flow direction. Thus, the presence of ACPs is crucial for contracting the network as a whole. A recent filament-level computational model for branched actin networks also included ACPs for achieving sufficient network connectivity [44].

Network disassembly at the rear in our model takes place in two different ways: F-actin depolymerization and severing. We found that these two dynamic events should take place at moderate rates at the rear to induce a steady retrograde flow without structural discontinuity or F-actin accumulation (Figs 3 and 4). In our model, we allowed F-actin depolymerization to occur only at the rear at a motor-independent rate although motors are present in the part of the region for actin depolymerization. It was experimentally shown that the depolymerization rate gradually increases towards the rear [26,57], which might be attributed to ATP hydrolysis of F-actins. It has been known that ADP-F-actin undergoes faster actin depolymerization and is more susceptible to depolymerization induced by cofilin [58–60]. We did not include a gradually changing depolymerization rate or ATP hydrolysis of actin for simplicity. Unlike depolymerization, F-actin severing can occur anywhere in our model. However, we assumed that the severing rate exponentially increases as a local bending angle on F-actin increases as in our previous studies [56,61]. This led to the dominant occurrence of F-actin severing at the rear because F-actins undergo buckling during network compaction into a bundle-like structure induced by motors, as we showed before [62]. In our previous study, we demonstrated that F-actin severing was indispensable for reproducing the pulsatile (i.e., reversible) contraction of actomyosin cortex observed in cells because the severing can locally increase the network disassembly rate within aggregating structures by creating more pointed ends where the depolymerization

takes place (Figs 4 and S6) [47]. Likewise, the buckling-induced severing helped the disassembly of the dense actin structure at the rear resulting from network accumulation.

Consistent with experimental studies, we found that larger force generation from more motors and less frictional forces from smaller FA region could result in a faster retrograde flow speed (Figs 5, 6, and S7) [20]. The importance of myosin motor activity and FAs has been demonstrated in many studies [28,63]. Contractile forces generated by motors contract the actin network toward the rear to drive a retrograde flow, whereas FAs resist the flow by exerting frictional forces via transient links formed between the underlying substrate and the network. Thus, the competition between the contractile forces and the frictional forces determines the nature and speed of the retrograde flow. We observed that the flow was negligible when motors could not overcome resistances from FAs. Once the contractile forces overcame the fractional forces from FAs, the flow speed abruptly increased due to frictional slippage between the network and the underlying substrate, which was shown in a previous study [63].

A recent study has shown that the mechanosensing ability of migrating cells allows them to adapt to different extracellular environments by adjusting the polymerization rate and density of F-actins in lamellipodia [64]. In addition, compressive loads were found to increase the density of growing filament ends in the branched actin network at the leading edge by decreasing the capping rate, instead of directly increasing an overall nucleation rate [65]. These experimental findings suggest that cells constantly adapt to time-varying environments by altering the activities and concentrations of key regulators. We showed that the branched network in lamellipodia can attain different modes of dynamic steady states (Fig 7). Specifically, we demonstrated that cases exhibiting a negligible retrograde flow due to one parameter can be rescued by varying other parameter value. For example, the case lacking contractile forces from motors could be rescued by decreasing the FA size. The case with a negligible retrograde flow due to rapid actin depolymerization could be rescued by enhancing the flow speed by including more motors or by decreasing the FA region.

Previous computational models of the lamellipodia have provided valuable insights into understanding the role of different molecular players. The molecular clutch model was developed to explain the actin retrograde flow driven by myosin activity and actin polymerization [63]. Although this one-dimensional model could capture the essential aspects of the retrograde flow, it was designed for representing filopodia, not lamellipodia. Thus, network connectivity mediated by Arp2/3 and ACPs, and network disassembly induced by buckling-induced severing could not be considered. Razbin et al. investigated the properties of a branched network in the lamellipodia, using a simple model where mother filaments grafted at one end undergo polymerization against a membrane at the leading edge [43]. Hu et al. developed a model incorporating physico-chemical reaction and diffusion processes in a stochastic manner [42]. Their model showed the importance of the interplay between F-actin, Arp2/3, and capping proteins for lamellipodial protrusion dynamics. However, these models aimed to probe the role of specific molecular players in protrusion dynamics rather than focusing on interactions between several key molecular players. Since they did not consider a competition between FAs and motor proteins, they could not capture the essential aspect of the lamellipodia. Schreiber et al. previously showed a three-dimensional stochastic model that reproduced the force-velocity relationship of cells observed experimentally [41]. Although this model was able to account for the retrograde flow in the lamellipodia, it comprised simplified actin dynamics, and the interplay between different factors, such as ACP binding, severing, and motor activity, was not considered.

Although our model captures key mechanical features of lamellipodial dynamics, it has several limitations that we plan to address in future work. First, our model does not consider a deformable cell membrane at the leading edge. In lamellipodia, the thermal fluctuation of the cell membrane randomly makes gap space between the membrane and the barbed ends of branches, allowing actin monomers to bind to the barbed ends of branches. This mechanism is referred to as the Brownian ratchet model [66]. The extension of this model, called the elastic Brownian ratchet, proposed that the bending fluctuation of actin filaments can generate sufficient gap space for monomer addition even when the filaments push against a rigid barrier [67,68]. While branches elongated by monomer addition can exert pushing forces to the membrane or the barrier, they also experience reaction forces, which can drive the retrograde flow. Our model does not explicitly simulate any of these

fluctuation-based mechanisms, so the contribution of the repulsive +y boundary to the retrograde flow is negligible. It means that the retrograde flow in our study is driven solely by motors located at the rear. In future work, we plan to include actin polymerization occurring against a rigid boundary or a deformable membrane that dynamically interacts with the barbed ends of branches, to better evaluate the relative contribution of actin polymerization to the retrograde flow. In the presence of polymerization-induced forces at the leading edge, the effects of parameters tested in this study could be different. For example, disconnection between the motor region and the network observed in many of our results would less likely occur if the network is pushed from the leading edge. However, F-actins located between the leading edge and the FA region can be buckled if friction exerted by the FA region is high, which would not take place if the network were pulled from the rear by motors.

In our model, regions of actin assembly, disassembly, adhesion, and motor activity are explicitly defined in fixed spatial zones, reflecting experimental observations that polymerization predominates at the leading edge, disassembly occurs at the rear, and myosin II is enriched at the interface between the lamellipodium and lamella. To more closely reflect physiological conditions, we plan to use a gradual spatial gradient of these processes (e.g., depolymerization rates increasing toward the rear) in our future work. In addition, the lamellipodium is considered as a closed system in our model, whereas in vivo, the actin pool is shared with the rest of the cell. This modeling choice leads to periodic cycling of actin density (e.g., Fig 2G), which is a natural outcome of monomer recycling in a closed system with a fixed actin pool and no external supply—a common assumption in agent-based cytoskeletal models. It is also important to note that to make actin dynamic more realistic, considering the explicit states of ATP-actin and ADP-actin with cofilin activity would be necessary. We also do not account for FA maturation and assumed instead that only nascent FAs are formed between the branched network and underlying substrate (Fig 2B).

We used actin concentration of 250 μM for reducing computational cost and assumed 90% of actin can be used for network assembly. This actin concentration is lower than ~500–1000 μM observed in lamellipodia via electron microscopy [57,69]. To compensate for the lack of connectivity between filaments due to lower actin concentration, we added a substantial number of ACPs and employed slightly longer F-actins, which could result in the formation of more bundles in the network. It is expected that our findings would be applicable to networks with higher actin concentration, fewer cross-linking proteins, and shorter filaments; networks would be still compacted into a bundle as observed in experiments [20]. In addition, depolymerization and severing will play a dominant role in filament disassembly because buckling will still take place during compaction by myosin activities.

Another limitation of this study is that wrinkle formation induced by myosin activities observed in lamellipodia or reconstituted actomyosin networks cannot be captured since there is no empty space above the network [70,71]; we observed that the network was formed in the entire z dimension of the computational domain (= 0.1 μm). However, since our model is intrinsically 3D, we may be able to reproduce the wrinkle pattern formation if we provide enough space above the network by increasing the z dimension of the domain. In addition, the fraction of actin monomers in this study, ~10%, is smaller than that in lamellipodia [57]. If this fraction is higher, the effect of the actin polymerization rate and Arp2/3 density would be different.

Conclusions

Our computational model successfully reproduced the actin retrograde flow of the branched network observed in the lamellipodia and provided insights into understanding the characteristics of the dynamic steady state of the flow. Our results suggested the importance of i) the balance between network assembly at the leading edge and network disassembly at rear and ii) a competition between myosin-generated contractile forces and FA-induced frictional forces acting between the network and a surrounding environment. We further demonstrated that different modes of dynamic steady states are possible, which sheds light on prior experimental findings about the adaptability of the lamellipodia to different mechanical environments. In this study, we focused on when the dynamic steady state can be maintained or disrupted mainly by showing retrograde flow speed and actin density. In a follow-up study, we would delve into several quantitative aspects of the dynamic state by performing additional quantitative measurements.

Materials and methods

Brownian dynamics via the Langevin equation

In our agent-based model, cytoskeletal elements consist of segments which are defined by their endpoints. The displacements of the endpoints of all segments are updated by the Langevin equation at each time step with inertia neglected:

$$\mathbf{F}_i - \zeta_i \frac{d\mathbf{r}_i}{dt} + \mathbf{F}_i^{\mathrm{T}} = 0 \tag{S1}$$

where $\mathbf{F}_i$, ζ_i, and $\mathbf{r}_i$ represent the deterministic forces, drag coefficient, and position vector of the ith endpoint, respectively, and t is time. ζ_i is calculated via an approximated form for a cylindrical object [72]:

$$\zeta_i = 3\pi\mu r_{c,i} \frac{3 + 2r_{0,i}/r_{c,i}}{5} \tag{S2}$$

where μ is the viscosity of the surrounding medium, and $r_{0,i}$ and $r_{c,i}$ are the length and diameter of segments, respectively. $\mathbf{F}^{\mathrm{T}}_i$ is a stochastic force satisfying the fluctuation-dissipation theorem [73]:

$$\left\langle \mathbf{F}_i^{\mathrm{T}}(t)\mathbf{F}_j^{\mathrm{T}}(t) \right\rangle = \frac{2k_B T\zeta_i \delta_{ij}}{\Delta t}\boldsymbol{\delta} \tag{S3}$$

where $\boldsymbol{\delta}$ is a second-order tensor, δ_{ij} is the Kronecker delta, $k_{\mathrm{B}}T$ is thermal energy, and $\Delta t = 1.15 \times 10^{-5}$ s is time step. The positions of the cylindrical segments are updated every time step using calculated velocities from the Langevin equation ($\mathrm{d}\mathbf{r}_i/\mathrm{d}t$) and the Euler integration scheme:

$$\mathbf{r}_i(t + \Delta t) = \mathbf{r}_i(t) + \frac{d\mathbf{r}_i}{dt}\Delta t = \mathbf{r}_i(t) + \frac{1}{\zeta_i}\left(\mathbf{F}_i + \mathbf{F}_i^{\mathrm{T}}\right)\Delta t \tag{S4}$$

For the deterministic forces, we consider i) extensional forces which maintain the equilibrium lengths of segments, ii) bending forces that maintain equilibrium angles formed by segments, iii) torsion forces which maintain torsional angles near their equilibrium values, and iv) repulsive forces which account for volume-exclusion effects between neighboring actin segments. The extensional, bending, and torsional forces are defined by the following potentials:

$$U_s = \frac{1}{2}\kappa_s (r - r_0)^2 \tag{S5}$$

$$U_b = \frac{1}{2}\kappa_b (\theta - \theta_0)^2 \tag{S6}$$

$$U_t = \frac{1}{2}\kappa_t (\phi - \phi_0)^2 \tag{S7}$$

where κ_{s}, κ_{b}, and κ_{t} represent the extensional, bending, and torsional stiffnesses, respectively. r and r_0 are the instantaneous and equilibrium lengths of segments, θ and θ_0 are instantaneous and equilibrium angles formed by interconnected segments, and ϕ and ϕ_0 are instantaneous and equilibrium torsional angles. The repulsive forces acting between F-actins are represented by the following harmonic potential [74]:

$$U_{r,A} = \begin{cases} \frac{1}{2}\kappa_{r,A}(r_{12} - r_{c,A})^2 & \text{if } r_{12} < r_{c,A} \\ 0 & \text{if } r_{12} \geq r_{c,A} \end{cases} \tag{S8}$$

where $\kappa_{r,A}$ represents the strength of repulsive forces, r_{12} is a distance between two neighboring elements, and $r_{c,A}$ is the diameter of actin segments.

Mechanics of cytoskeletal components

The extensional ($\kappa_{s,A}$) and bending ($\kappa_{b,A}$) stiffnesses of actin segments maintain their equilibrium length ($r_{0,A} = 140$ nm) and equilibrium angle ($\theta_{0,A} = 0$ rad), respectively (S1 Fig). The equilibrium length of each ACP segment ($r_{0,ACP} = 20$ nm) and an equilibrium angle between two ACP segments ($\theta_{0,ACP} = 0$ rad) are maintained by extensional ($\kappa_{s,ACP}$) and bending ($\kappa_{b,ACP}$) stiffnesses, respectively.

Arp2/3 is involved with one extensional stiffness, four bending stiffnesses, and one torsional stiffness. The equilibrium length of each Arp2/3 segment ($r_{0,Arp2/3} = 35$ nm) is maintained by extensional stiffness ($\kappa_{s,Arp2/3}$). An equilibrium angle between two Arp2/3 segments ($\theta_{0,Arp2/3} = 0$ rad) is maintained by bending stiffness ($\kappa_{b,Arp2/3c}$). Two bending stiffnesses ($\kappa_{b,Arp2/3m}$ and $\kappa_{b,Arp2/3d}$) maintain an equilibrium angle between one segment of Arp2/3 and the mother filament ($\theta_{0,Arp2/3m} = 90° = 1.57$ rad) and an equilibrium angle between the other segment of Arp2/3 and the daughter filament ($\theta_{0,Arp2/3d} = 20° = 0.35$ rad), respectively. Another bending stiffness ($\kappa_{b,Arp2/3f}$) maintains an equilibrium angle between the mother and daughter filaments ($\theta_{0,Arp2/3d} = 70° = 1.22$ rad). Torsional stiffness ($\kappa_{t,Arp2/3}$) maintains a zero torsional angle between the mother and daughter filaments to enforce them to exist on a single plane.

The equilibrium length of motor backbone segments ($r_{s,MB} = 42$ nm) and an equilibrium angle between the backbone segments ($\theta_{s,MB} = 0$ rad) are maintained by bending ($\kappa_{b,MB}$) and extensional ($\kappa_{s,MB}$) stiffnesses, respectively. The value of $\kappa_{s,MB}$ is equal to $\kappa_{s,A}$, whereas the value of $\kappa_{b,MB}$ is much greater than $\kappa_{b,A}$. The extension of each motor arm is regulated by the two-spring model with the stiffnesses of transverse ($\kappa_{s,M1}$) and longitudinal ($\kappa_{s,M2}$) springs. The transverse spring maintains an equilibrium distance ($r_{0,M1} = 10$ nm) between the endpoint of a motor backbone and an actin segment where the arm of the motor binds, and the longitudinal spring helps maintain the right angle between the motor arm and the actin segment ($r_{0,M2} = 0$ nm).

Dynamic behaviors of cytoskeletal components

F-actin can undergo de novo nucleation, polymerization, depolymerization, and angle-dependent severing. The de novo nucleation occurs via the appearance of a single actin segment at $z = 0$ with a constant rate constant, $k_{n,A}$. The orientation of the segment is perpendicular to the z direction, meaning that the segment belongs to xy plane. Actin polymerization occurs only from the barbed end of F-actin with a constant rate constant, $k_{+,A}$, by adding one segment. Actin depolymerization takes place only from the pointed end of F-actin at a constant rate, $k_{-,A}$, by removing one segment. Both polymerization and depolymerization occur without dependence on force. F-actin is not allowed to elongate beyond 0.98 μm to mimic the activity of capping proteins [15,75]. F-actin severing occurs with a rate, k_{sev}, proportional to a local bending angle by removing one segment at the mid of F-actin:

$$k_{sev} = k_{0,sev} \exp\left(\lambda_{sev}\theta\right) \tag{S9}$$

where $k_{0,sev}$ and λ_{sev} represent the zero-angle severing rate constant and angle sensitivity, respectively [76]. This equation was adopted from our previous study [61] where we reproduced the distribution of angles at which severing occurred during thermal fluctuation of F-actin observed in experiments [46]. Since the value of $k_{0,sev}$ is extremely low, severing can take place only when the local bending angle of F-actin becomes large due to buckling induced by myosin activities.

ACPs connect pairs of F-actins to form functional cross-linking points. They bind to binding sites located on F-actins every 7 nm first with a constant rate constant, $k_{+,ACP}$, and then bind to binding sites on the other F-actin with the same rate constant if they are sufficiently proximal to each other. Unlike our previous studies [62,77], it is assumed that ACPs cannot unbind from F-actins by themselves, meaning that they form permanent cross-links.

Arp2/3 binds to binding sites on F-actins with a constant rate constant, $k_{+,Arp2/3}$. Immediately after binding, it nucleates a daughter filament; a new actin segment appears with the characteristic angle of 70° relative to the mother filament with a directional bias towards the leading edge. Connections between Arp2/3 and mother/daughter filaments are assumed to be permanent.

Motor arms bind to binding sites on actin segments with the rate of $40N_h$ where N_h is the number of myosin heads represented by one motor arm. After binding, motor arms are able to walk along F-actin at a force-dependent rate, $k_{w,M}$, and unbind from actin segments at a force-dependent rate, $k_{u,M}$. $k_{w,M}$ and $k_{u,M}$ are determined by the parallel cluster model to account for the mechanochemical cycle of non-muscle myosin II [11,48,49,6]. Details of implementation and benchmarking of the parallel cluster model were described in our previous study [78]. The parallel cluster model assumes three states of myosin heads and uses 5 transition rates between those states. One of them is the ATP-dependent unbinding rate of myosin heads (k_{20}) which defines a transition rate from the post power stroke state to the unbound state. $k_{w,M}$ and $k_{u,M}$ in the model are lower with smaller k_{20} or with a larger applied load due to an assumption that motors exhibit a catch-bond behavior. The unloaded walking velocity and stall force of motor arms with the reference value of k_{20} are set to 120 nm/s and 5.33 pN, respectively. If all arms of a motor lose connection to F-actin, its backbone is disassembled instantaneously and assembled on F-actin in a different location. The backbone assembly cannot occur if there is no F-actin to bind within the motor region. Thus, the number of motors may look different on snapshots between cases even if the motor density is identical.

In case of depolymerization or severing of F-actin, Arp2/3, ACPs, and motor arms bound to a disappearing actin segment lose one connection to F-actin. Then, they are able to bind to a new binding site on F-actin.

Models for a substrate and nascent focal adhesions

A substrate underlying the network is coarse-grained into a two-dimensional triangulated mesh (Fig 1B). Extensional stiffness ($\kappa_{s,sub}$) maintains the length of chains between mesh nodes near their equilibrium length ($r_{0,sub} = 50$ nm). Bending stiffness ($\kappa_{b,sub}$) maintains an angle formed by mesh nodes near its equilibrium value ($\theta_{0,sub} = 60° = 1.05$ rad). The movement of mesh nodes in the z direction is not allowed, constraining the substrate as a plane located at $z = 0$. In our previous study [16], we have explored the effect of a variation in either of $\kappa_{s,sub}$, $\kappa_{b,sub}$, or $r_{0,sub}$ on the substrate stiffness, κ_{eff}. κ_{eff} was found to be proportional to $\kappa_{s,sub}$ and $\kappa_{b,sub}$ but inversely proportional to $r_{0,sub}$. With parameter values that we use in this study ($\kappa_{s,sub} = 1.0 \times 10^{-4}$ N/m, $\kappa_{b,sub} = 2.4 \times 10^{-20}$ Nm, $r_{0,sub} = 5.0 \times 10^{-8}$ m), κ_{eff} is $\sim 2.4 \times 10^{-4}$ N/m. Thus, the substrate used in this model is considered rather soft.

To mimic the formation of nascent FAs, each mesh node is able to form a single link with any endpoint of actin segments at the rate of $k_{+,C}$ if they are located within 200 nm. Then, this link behaves as an elastic linear spring whose equilibrium length is equal to the initial length of the link. Extensional stiffness ($\kappa_{s,C}$) maintains the equilibrium length of the link, and each link is considered as a nascent FA site, hindering the retrograde flow caused by motor activity. These links can break at a force-dependent rate, $k_{u,C}$:

$$k_{u,C} = \begin{cases} k^0_{u,C} \exp\left(\frac{\lambda_{u,C}|\mathbf{F}_{s,C}|}{k_B T}\right) & \text{if } r \geq r_{0,C} \\ k^0_{u,C} & \text{if } r < r_{0,C} \end{cases} \quad \text{(S10)}$$

where $k^0_{u,C}$ and $\lambda_{u,C}$ represent the zero-force unbinding rate constant and force sensitivity, respectively, and $\mathbf{F}_{s,C}$ is a spring force acting on the link. r and $r_{0,C}$ are instantaneous and equilibrium lengths of the link, respectively.

Computational setup

To simulate the sheet-like, flat geometry of lamellipodia, a relatively wide and thin three-dimensional domain with the dimensions of $5 \times 2.5 \times 0.1$ μm in x, y, and z directions is employed. Periodic boundary conditions are applied in the x

direction, whereas boundaries normal to the y and z directions exert repulsive forces to elements that are displaced out of the domain. The + y boundary represents the leading edge, and the -y boundary corresponds to the interface between lamellipodia and lamella. We do not consider a movable membrane on the leading edge for simplicity. A triangular mesh is created at z = 0 as an underlying substrate. A branched network is formed via self-assembly of F-actin, Arp2/3, and ACP, with the barbed ends of F-actins biased toward +y direction. Specifically, the actin network is created from the -y boundary via the de novo nucleation of seed filaments with their barbed ends directed toward the + y direction. Although lamellipodia are assembled from the leading edge and grow in the -y direction in cells, a resultant network structure is similar. F-actins are elongated up to 0.98 μm via polymerization and form branches via the side binding of Arp2/3. Only ~90% of actin segments are used for network assembly to leave some free segments. ACPs physically interconnect F-actins to increase network connectivity. To reflect the primary location of myosin motors at the interface between the lamellipodia and lamella [30], we specified a region near the -y boundary (y = 0 – 0.1875 μm) for motor activity with binding, walking, and unbinding. To prevent motors from drifting toward the + y boundary, we reduced the mobility of motors by increasing their drag coefficient 1000-fold relative to a value calculated via Eq. S2.

After network formation, motors walk along F-actins toward the barbed end to contract the network toward the -y boundary. To allow for a continuous actin retrograde flow, F-actins are depolymerized from their pointed ends in a region near the -y boundary (y = 0 – 0.375 μm), whereas they are polymerized from their barbed ends in a region near the + y boundary (y = 2.125 – 2.5 μm). Free actin segments generated from depolymerization and severing of F-actins are used for polymerization at the leading edge. Reference parameter values are selected to reproduce physiologically relevant retrograde flow speed. Under the reference condition, actin concentration (C_A) is 250 μM, ACP density (R_{ACP}) is 0.04, Arp2/3 density ($R_{Arp2/3}$) is 0.01, and motor density (R_M) is 0.004. Note that for computational efficiency, actin concentration of 250 μM we use in this study is lower than ~500–1000 μM measured in the real lamellipodia via electron microscopy [57,69]. We performed simulations for 300 s with a change in parameter values. The reference values for all parameters are listed in S1 Table.

Measurement, analysis, and network visualization

The retrograde flow speed is calculated every 2 s. The calculation is done using the y component of the velocities of F-actins located within a rectangular region near the + y boundary (Fig 1C).

F-actin density is calculated every 1 s. First, the domain is divided into 40 subdomains in the y direction. In each subdomain, the number of actin segments is divided by $N_A/40$, where N_A is the total number of actin segments in an entire domain. If actin segments are uniformly distributed, this normalized value would be close to 1. The heterogeneity of the network morphology was quantified by the coefficient of variation of F-actin density in the y direction; a lower value from this calculation indicates a more homogenous network.

Forces acting between the substrate and the network are calculated using links forming between membrane nodes and F-actins. Using the equilibrium length and spring constant of links (S1 Table), individual forces acting on each nascent FA are calculated in each time step. The total substrate force is calculated by summing up forces acting on all links.

F-actin, Arp2/3, ACP, motor, and underlying substrate are visualized using Visual Molecular Dynamics (VMD, University of Illinois at Urbana-Champaign).

Supporting information

S1 Fig. Schematics showing stiffness parameters for each cytoskeletal component in the model. (A) F-actin, (B) ACP, (C) Arp2/3 complex, and (D) motor. κ_b and κ_s indicate bending and extensional stiffnesses that maintain equilibrium angles and lengths, respectively. In (C), the torsional stiffness is not included in the schematic. Detailed descriptions about these stiffness parameters and their values are written in S1 Table.
(TIFF)

S2 Fig. Deficient actin polymerization disrupts a continuous retrograde flow. (A, B) Snapshots of the branched network taken at ~150 s with a lower (0.4 $\mu M^{-1}s^{-1}$) or higher (24 $\mu M^{-1}s^{-1}$) polymerization rate constant ($k_{+,A}$) than that of the reference case, 12 $\mu M^{-1}s^{-1}$. (C, D) Kymographs of actin concentration as a function of y position and time with different $k_{+,A}$. With lower $k_{+,A}$, network heterogeneity increased because the network was contracted toward the -y boundary before sufficient F-actins were assembled near the + y boundary. (E) Heterogeneity of the network quantified as a coefficient of variation in actin density in the y direction. The network was more heterogeneous with deficient actin polymerization. (F) Retrograde flow speed depending on $k_{+,A}$. With deficient actin polymerization, flow speed is lower, and the network failed to reach steady state. (G) Time evolution of retrograde flow speed.
(TIFF)

S3 Fig. Sufficiently high Arp2/3 density is required to maintain the continuity of branched network architecture. (A, B) Snapshots of the branched network taken at ~150 s with a lower (0.006) or higher (0.016) Arp2/3 density ($R_{Arp2/3}$) relative to that of the reference condition, 0.01. (C, D) Kymographs of actin concentration as a function of y position and time with different $R_{Arp2/3}$. With low $R_{Arp2/3}$, the network could not grow sufficiently, leading to higher network heterogeneity and lack of continuity in the y direction. By contrast, high $R_{Arp2/3}$ resulted in the formation of more branches on a fraction of vertically growing structures, so the network became more heterogeneous with lower connectivity in the x direction. (E) Heterogeneity of the network quantified as a coefficient of variation in actin density in the y direction. (F) Retrograde flow speed with different $R_{Arp2/3}$. A decrease in the flow speed was noticeable at $R_{Arp2/3} < 0.01$. (G) Time evolution of retrograde flow speed.
(TIFF)

S4 Fig. More actin crosslinking proteins (ACPs) enhance network connection and thus lead to a continuous flow and homogeneous network morphology. (A, B) Snapshots showing the branched network taken at ~150 s with a lower (0.005) or higher (0.08) R_{ACP} relative to that of the reference condition, 0.04. (C, D) Kymographs of actin concentration as a function of y position and time with different R_{ACP}. With higher R_{ACP}, the network showed more homogeneous morphology and a continuous flow. (E) Heterogeneity of the network quantified as a coefficient of variation in actin density in the y direction. (F) Retrograde flow speed with different R_{ACP}. With low R_{ACP} values, network heterogeneity was higher, and flow speed was slower. (G) Time evolution of retrograde flow speed.
(TIFF)

S5 Fig. Time evolution of retrograde flow speed with a change in various parameters. (A) Actin depolymerization rate ($k_{-,A}$). (B) Actin severing rate constant ($k_{0,sev}$). (C) Motor density (R_M). (D) Relative size of FA region (A_{FA}).
(TIFF)

S6 Fig. Effects of the angle sensitivity of F-actin severing (λ_{sev}). (A, B) Snapshots of the branched network taken at ~150 s with lower (0.5 deg^{-1}) or higher (2.5 deg^{-1}) λ_{sev} relative to that of the reference condition, 1.0 deg^{-1}. (C, D) Kymographs of actin concentration as a function of y position and time with different λ_{sev}. (E) Heterogeneity of the network quantified as a coefficient of variation in actin density in the y direction. (F) Retrograde flow speed with different λ_{sev}. Cases with intermediate λ_{sev} reached a steady state with faster flow speed and homogenous network. (G) Time evolution of retrograde flow speed.
(TIFF)

S7 Fig. Effect of the ATP-dependent unbinding rate of myosin heads (k_{20}) on a steady state. With higher k_{20}, walking speed tends to be higher. (A, B) Snapshots of the branched network taken at ~150 s with lower (2 s^{-1}) or higher (30 s^{-1}) k_{20} relative to that of the reference condition, 17 s^{-1}. (C, D) Kymographs of averaged actin concentration as a function of y position and time with lower or higher k_{20}. With the lowest k_{20}, the network was disconnected from motors due to excessively slow flow speed. (E) Heterogeneity of the network quantified as a coefficient of variation in actin density in

the y direction. (F) Retrograde flow speed with different k_{20}. (G) Time evolution of retrograde flow speed. (H) Total force acting on the substrate by the network with different k_{20}. Flow speed and total substrate force were proportional to k_{20} at $k_{20} \leq 17\,s^{-1}$ and reached a plateau at $k_{20} > 17\,s^{-1}$.
(TIFF)

S1 Table. List of parameters used for the lamellipodium model. Some of the parameters with references were determined using experimental measurements. Other parameters were determined based on our prior studies [16,77,79]. Each of key parameters tested in this study was tested before the reference case was identified.
(PDF)

S1 Movie. Steady-state dynamics of a branched network under the reference condition. The network architecture remained homogeneous and maintained continuity over 300 seconds.
(MP4)

Author contributions

Formal analysis: June Hyung Kim.

Funding acquisition: Taeyoon Kim.

Investigation: June Hyung Kim, Taeyoon Kim.

Project administration: Taeyoon Kim.

Supervision: Taeyoon Kim.

Visualization: June Hyung Kim.

Writing – original draft: June Hyung Kim.

Writing – review & editing: Taeyoon Kim.

References

1. Carmona G, Perera U, Gillett C, Naba A, Law A-L, Sharma VP, et al. Lamellipodin promotes invasive 3D cancer cell migration via regulated interactions with Ena/VASP and SCAR/WAVE. Oncogene. 2016;35(39):5155–69. https://doi.org/10.1038/onc.2016.47 PMID: 26996666
2. Machesky LM. Lamellipodia and filopodia in metastasis and invasion. FEBS Lett. 2008;582(14):2102–11. https://doi.org/10.1016/j.febslet.2008.03.039 PMID: 18396168
3. Trepat X, Wasserman MR, Angelini TE, Millet E, Weitz DA, Butler JP, et al. Physical forces during collective cell migration. Nature Phys. 2009;5(6):426–30. https://doi.org/10.1038/nphys1269
4. Amann KJ, Pollard TD. The Arp2/3 complex nucleates actin filament branches from the sides of pre-existing filaments. Nat Cell Biol. 2001;3(3):306–10. https://doi.org/10.1038/35060104 PMID: 11231582
5. Bieling P, Rottner K. From WRC to Arp2/3: Collective molecular mechanisms of branched actin network assembly. Current Opinion in Cell Biology. 2023;80:102156. https://doi.org/10.1016/j.ceb.2023.102156
6. Gautreau AM, Fregoso FE, Simanov G, Dominguez R. Nucleation, stabilization, and disassembly of branched actin networks. Trends Cell Biol. 2022;32(5):421–32. https://doi.org/10.1016/j.tcb.2021.10.006 PMID: 34836783
7. Ryan GL, Holz D, Yamashiro S, Taniguchi D, Watanabe N, Vavylonis D. Cell protrusion and retraction driven by fluctuations in actin polymerization: A two-dimensional model. Cytoskeleton (Hoboken). 2017;74(12):490–503. https://doi.org/10.1002/cm.21389 PMID: 28752950
8. Dang I, Gorelik R, Sousa-Blin C, Derivery E, Guérin C, Linkner J, et al. Inhibitory signalling to the Arp2/3 complex steers cell migration. Nature. 2013;503(7475):281–4. https://doi.org/10.1038/nature12611 PMID: 24132237
9. Waterman-Storer CM, Worthylake RA, Liu BP, Burridge K, Salmon ED. Microtubule growth activates Rac1 to promote lamellipodial protrusion in fibroblasts. Nat Cell Biol. 1999;1(1):45–50. https://doi.org/10.1038/9018 PMID: 10559863
10. Fletcher DA, Mullins RD. Cell mechanics and the cytoskeleton. Nature. 2010;463(7280):485–92. https://doi.org/10.1038/nature08908 PMID: 20110992
11. Machesky LM, Mullins RD, Higgs HN, Kaiser DA, Blanchoin L, May RC, et al. Scar, a WASp-related protein, activates nucleation of actin filaments by the Arp2/3 complex. Proc Natl Acad Sci U S A. 1999;96(7):3739–44. https://doi.org/10.1073/pnas.96.7.3739 PMID: 10097107

12. Mehidi A, Kage F, Karatas Z, Cercy M, Schaks M, Polesskaya A, et al. Forces generated by lamellipodial actin filament elongation regulate the WAVE complex during cell migration. Nat Cell Biol. 2021;23(11):1148–62. https://doi.org/10.1038/s41556-021-00786-8 PMID: 34737443
13. Mullins RD, Heuser JA, Pollard TD. The interaction of Arp2/3 complex with actin: nucleation, high affinity pointed end capping, and formation of branching networks of filaments. Proc Natl Acad Sci U S A. 1998;95(11):6181–6. https://doi.org/10.1073/pnas.95.11.6181 PMID: 9600938
14. Goley ED, Welch MD. The ARP2/3 complex: an actin nucleator comes of age. Nat Rev Mol Cell Biol. 2006;7(10):713–26. https://doi.org/10.1038/nrm2026 PMID: 16990851
15. Sinnar SA, Antoku S, Saffin J-M, Cooper JA, Halpain S. Capping protein is essential for cell migration in vivo and for filopodial morphology and dynamics. Mol Biol Cell. 2014;25(14):2152–60. https://doi.org/10.1091/mbc.E13-12-0749 PMID: 24829386
16. Mair DB, Elmasli C, Kim JH, Barreto AD, Ding S, Gu L, et al. The Arp2/3 complex enhances cell migration on elastic substrates. Mol Biol Cell. 2023;34(7):ar67. https://doi.org/10.1091/mbc.E22-06-0243 PMID: 36989030
17. Falzone TT, Lenz M, Kovar DR, Gardel ML. Assembly kinetics determine the architecture of α-actinin crosslinked F-actin networks. Nat Commun. 2012;3:861. https://doi.org/10.1038/ncomms1862 PMID: 22643888
18. Kasza KE, Broedersz CP, Koenderink GH, Lin YC, Messner W, Millman EA, et al. Actin filament length tunes elasticity of flexibly cross-linked actin networks. Biophys J. 2010;99(4):1091–100. https://doi.org/10.1016/j.bpj.2010.06.025 PMID: 20712992
19. Schaefer AW, Kabir N, Forscher P. Filopodia and actin arcs guide the assembly and transport of two populations of microtubules with unique dynamic parameters in neuronal growth cones. J Cell Biol. 2002;158(1):139–52. https://doi.org/10.1083/jcb.200203038 PMID: 12105186
20. Burnette DT, Manley S, Sengupta P, Sougrat R, Davidson MW, Kachar B, et al. A role for actin arcs in the leading-edge advance of migrating cells. Nat Cell Biol. 2011;13(4):371–81. https://doi.org/10.1038/ncb2205 PMID: 21423177
21. McGough A, Pope B, Chiu W, Weeds A. Cofilin changes the twist of F-actin: implications for actin filament dynamics and cellular function. J Cell Biol. 1997;138(4):771–81. https://doi.org/10.1083/jcb.138.4.771 PMID: 9265645
22. Maciver SK, Hussey PJ. The ADF/cofilin family: actin-remodeling proteins. Genome Biol. 2002;3(5):reviews3007. https://doi.org/10.1186/gb-2002-3-5-reviews3007 PMID: 12049672
23. McCullagh M, Saunders MG, Voth GA. Unraveling the mystery of ATP hydrolysis in actin filaments. J Am Chem Soc. 2014;136(37):13053–8. https://doi.org/10.1021/ja507169f PMID: 25181471
24. Goode BL, Eskin J, Shekhar S. Mechanisms of actin disassembly and turnover. J Cell Biol. 2023;222(12):e202309021. https://doi.org/10.1083/jcb.202309021 PMID: 37948068
25. Blanchoin L, Boujemaa-Paterski R, Sykes C, Plastino J. Actin dynamics, architecture, and mechanics in cell motility. Physiol Rev. 2014;94(1):235–63. https://doi.org/10.1152/physrev.00018.2013 PMID: 24382887
26. Pollard TD, Borisy GG. Cellular motility driven by assembly and disassembly of actin filaments. Cell. 2003;112(4):453–65. https://doi.org/10.1016/s0092-8674(03)00120-x PMID: 12600310
27. Wilson CA, Tsuchida MA, Allen GM, Barnhart EL, Applegate KT, Yam PT, et al. Myosin II contributes to cell-scale actin network treadmilling through network disassembly. Nature. 2010;465(7296):373–7. https://doi.org/10.1038/nature08994 PMID: 20485438
28. Gardel ML, Sabass B, Ji L, Danuser G, Schwarz US, Waterman CM. Traction stress in focal adhesions correlates biphasically with actin retrograde flow speed. J Cell Biol. 2008;183(6):999–1005. https://doi.org/10.1083/jcb.200810060 PMID: 19075110
29. Yamashiro S, Watanabe N. A new link between the retrograde actin flow and focal adhesions. J Biochem. 2014;156(5):239–48. https://doi.org/10.1093/jb/mvu053 PMID: 25190817
30. Giannone G, Dubin-Thaler BJ, Rossier O, Cai Y, Chaga O, Jiang G, et al. Lamellipodial actin mechanically links myosin activity with adhesion-site formation. Cell. 2007;128(3):561–75. https://doi.org/10.1016/j.cell.2006.12.039 PMID: 17289574
31. Murrell M, Oakes PW, Lenz M, Gardel ML. Forcing cells into shape: the mechanics of actomyosin contractility. Nat Rev Mol Cell Biol. 2015;16(8):486–98. https://doi.org/10.1038/nrm4012 PMID: 26130009
32. Krishna A, Savinov M, Ierushalmi N, Mogilner A, Keren K. Size-dependent transition from steady contraction to waves in actomyosin networks with turnover. Nat Phys. 2024;20(1):123–34. https://doi.org/10.1038/s41567-023-02271-5
33. Gat S, Amit Y, Livne G, Sanchez DS, Porat N, Yochelis A, et al. Actin turnover and myosin contractility determine emergent thickness robustness of cell-mimicking cortex. bioRxiv. 2024. https://doi.org/10.1101/2024.11.04.621887
34. Malik-Garbi M, Ierushalmi N, Jansen S, Abu-Shah E, Goode BL, Mogilner A, et al. Scaling behaviour in steady-state contracting actomyosin networks. Nat Phys. 2019;15(5):509–16. https://doi.org/10.1038/s41567-018-0413-4 PMID: 31754369
35. Sonal, Ganzinger KA, Vogel SK, Mücksch J, Blumhardt P, Schwille P. Myosin-II activity generates a dynamic steady state with continuous actin turnover in a minimal actin cortex. J Cell Sci. 2018;132(4):jcs219899. https://doi.org/10.1242/jcs.219899 PMID: 30538127
36. Wu Z, Plotnikov SV, Moalim AY, Waterman CM, Liu J. Two distinct actin networks mediate traction oscillations to confer focal adhesion mechanosensing. Biophys J. 2017;112(4):780–94. https://doi.org/10.1016/j.bpj.2016.12.035 PMID: 28256237
37. Craig EM, Stricker J, Gardel M, Mogilner A. Model for adhesion clutch explains biphasic relationship between actin flow and traction at the cell leading edge. Phys Biol. 2015;12(3):035002. https://doi.org/10.1088/1478-3975/12/3/035002 PMID: 25969948

38. Raz-Ben Aroush D, Ofer N, Abu-Shah E, Allard J, Krichevsky O, Mogilner A, et al. Actin Turnover in Lamellipodial Fragments. Curr Biol. 2017;27(19):2963-2973.e14. https://doi.org/10.1016/j.cub.2017.08.066 PMID: 28966086
39. Chen X, Zhu H, Feng X, Li X, Lu Y, Wang Z, et al. Predictive assembling model reveals the self-adaptive elastic properties of lamellipodial actin networks for cell migration. Commun Biol. 2020;3(1):616. https://doi.org/10.1038/s42003-020-01335-z PMID: 33106551
40. Schmeiser C, Winkler C. The flatness of Lamellipodia explained by the interaction between actin dynamics and membrane deformation. Journal of Theoretical Biology. 2015;380:144–55. https://doi.org/10.1016/j.jtbi.2015.05.010
41. Schreiber CH, Stewart M, Duke T. Simulation of cell motility that reproduces the force-velocity relationship. Proc Natl Acad Sci U S A. 2010;107(20):9141–6. https://doi.org/10.1073/pnas.1002538107 PMID: 20439759
42. Hu L, Papoian GA. Mechano-chemical feedbacks regulate actin mesh growth in lamellipodial protrusions. Biophys J. 2010;98(8):1375–84. https://doi.org/10.1016/j.bpj.2009.11.054 PMID: 20409456
43. Razbin M, Falcke M, Benetatos P, Zippelius A. Mechanical properties of branched actin filaments. Phys Biol. 2015;12(4):046007. https://doi.org/10.1088/1478-3975/12/4/046007 PMID: 26040560
44. Rutkowski DM, Vavylonis D. Discrete mechanical model of lamellipodial actin network implements molecular clutch mechanism and generates arcs and microspikes. PLoS Comput Biol. 2021;17(10):e1009506. https://doi.org/10.1371/journal.pcbi.1009506 PMID: 34662335
45. Haviv L, Gillo D, Backouche F, Bernheim-Groswasser A. A cytoskeletal demolition worker: myosin II acts as an actin depolymerization agent. J Mol Biol. 2008;375(2):325–30. https://doi.org/10.1016/j.jmb.2007.09.066 PMID: 18021803
46. McCullough BR, Grintsevich EE, Chen CK, Kang H, Hutchison AL, Henn A, et al. Cofilin-linked changes in actin filament flexibility promote severing. Biophys J. 2011;101(1):151–9. https://doi.org/10.1016/j.bpj.2011.05.049 PMID: 21723825
47. Yu Q, Li J, Murrell MP, Kim T. Balance between Force Generation and Relaxation Leads to Pulsed Contraction of Actomyosin Networks. Biophys J. 2018;115(10):2003–13. https://doi.org/10.1016/j.bpj.2018.10.008 PMID: 30389091
48. Erdmann T, Albert PJ, Schwarz US. Stochastic dynamics of small ensembles of non-processive molecular motors: the parallel cluster model. J Chem Phys. 2013;139(17):175104. https://doi.org/10.1063/1.4827497 PMID: 24206337
49. Erdmann T, Schwarz US. Stochastic force generation by small ensembles of myosin II motors. Phys Rev Lett. 2012;108(18). https://doi.org/10.1103/physrevlett.108.188101
50. Johnson CA, Walklate J, Svicevic M, Mijailovich SM, Vera C, Karabina A, et al. The ATPase cycle of human muscle myosin II isoforms: Adaptation of a single mechanochemical cycle for different physiological roles. J Biol Chem. 2019;294(39):14267–78. https://doi.org/10.1074/jbc.RA119.009825 PMID: 31387944
51. Cuda G, Pate E, Cooke R, Sellers JR. In vitro actin filament sliding velocities produced by mixtures of different types of myosin. Biophysical Journal. 1997;72(4):1767–79. https://doi.org/10.1016/s0006-3495(97)78823-4
52. Yamashiro S, Mizuno H, Smith MB, Ryan GL, Kiuchi T, Vavylonis D, et al. New single-molecule speckle microscopy reveals modification of the retrograde actin flow by focal adhesions at nanometer scales. Mol Biol Cell. 2014;25(7):1010–24. https://doi.org/10.1091/mbc.E13-03-0162 PMID: 24501425
53. Alexandrova AY, Arnold K, Schaub S, Vasiliev JM, Meister J-J, Bershadsky AD, et al. Comparative dynamics of retrograde actin flow and focal adhesions: formation of nascent adhesions triggers transition from fast to slow flow. PLoS One. 2008;3(9):e3234. https://doi.org/10.1371/journal.pone.0003234 PMID: 18800171
54. Mueller J, Szep G, Nemethova M, de Vries I, Lieber AD, Winkler C, et al. Load Adaptation of Lamellipodial Actin Networks. Cell. 2017;171(1):188-200.e16. https://doi.org/10.1016/j.cell.2017.07.051 PMID: 28867286
55. Papalazarou V, Machesky LM. The cell pushes back: The Arp2/3 complex is a key orchestrator of cellular responses to environmental forces. Curr Opin Cell Biol. 2021;68:37–44. https://doi.org/10.1016/j.ceb.2020.08.012 PMID: 32977244
56. Li J, Biel T, Lomada P, Yu Q, Kim T. Buckling-induced F-actin fragmentation modulates the contraction of active cytoskeletal networks. Soft Matter. 2017;13(17):3213–20. https://doi.org/10.1039/c6sm02703b PMID: 28398452
57. Koestler SA, Rottner K, Lai F, Block J, Vinzenz M, Small JV. F- and G-actin concentrations in lamellipodia of moving cells. PLoS One. 2009;4(3):e4810. https://doi.org/10.1371/journal.pone.0004810 PMID: 19277198
58. Pollard TD. Polymerization of ADP-actin. J Cell Biol. 1984;99(3):769–77. https://doi.org/10.1083/jcb.99.3.769 PMID: 6540783
59. Fujiwara I, Vavylonis D, Pollard TD. Polymerization kinetics of ADP- and ADP-Pi-actin determined by fluorescence microscopy. Proc Natl Acad Sci U S A. 2007;104(21):8827–32. https://doi.org/10.1073/pnas.0702510104 PMID: 17517656
60. Kudryashov DS, Reisler E. ATP and ADP actin states. Biopolymers. 2013;99(4):245–56. https://doi.org/10.1002/bip.22155 PMID: 23348672
61. Jung W, Murrell MP, Kim T. F-actin fragmentation induces distinct mechanisms of stress relaxation in the actin cytoskeleton. ACS Macro Lett. 2016;5(6):641–5. https://doi.org/10.1021/acsmacrolett.6b00232 PMID: 35614663
62. Bidone TC, Jung W, Maruri D, Borau C, Kamm RD, Kim T. Morphological transformation and force generation of active cytoskeletal networks. PLoS Comput Biol. 2017;13(1):e1005277. https://doi.org/10.1371/journal.pcbi.1005277 PMID: 28114384
63. Chan CE, Odde DJ. Traction dynamics of filopodia on compliant substrates. Science. 2008;322(5908):1687–91. https://doi.org/10.1126/science.1163595 PMID: 19074349

64. Chen X, Li Y, Guo M, Xu B, Ma Y, Zhu H, et al. Polymerization force-regulated actin filament-Arp2/3 complex interaction dominates self-adaptive cell migrations. Proc Natl Acad Sci U S A. 2023;120(36):e2306512120. https://doi.org/10.1073/pnas.2306512120 PMID: 37639611
65. Li T-D, Bieling P, Weichsel J, Mullins RD, Fletcher DA. The molecular mechanism of load adaptation by branched actin networks. eLife. 2022;11. https://doi.org/10.7554/elife.73145
66. Watanabe N. Brownian ratchet force sensor at the contacting point between F-actin barbed end and lamellipodium tip plasma membrane. In: Suetsugu S, editor. Plasma Membrane Shaping. Academic Press;. 2023. p. 295–306. https://doi.org/10.1016/b978-0-323-89911-6.00015-7
67. Mogilner A, Oster G. Force generation by actin polymerization II: the elastic ratchet and tethered filaments. Biophys J. 2003;84(3):1591–605. https://doi.org/10.1016/S0006-3495(03)74969-8 PMID: 12609863
68. Mogilner A, Oster G. Cell motility driven by actin polymerization. Biophys J. 1996;71(6):3030–45. https://doi.org/10.1016/S0006-3495(96)79496-1 PMID: 8968574
69. Watanabe K. Unique features of animal mitochondrial translation systems. The non-universal genetic code, unusual features of the translational apparatus and their relevance to human mitochondrial diseases. Proc Jpn Acad Ser B Phys Biol Sci. 2010;86(1):11–39. https://doi.org/10.2183/pjab.86.11 PMID: 20075606
70. Livne G, Gat S, Armon S, Bernheim-Groswasser A. Self-assembled active actomyosin gels spontaneously curve and wrinkle similar to biological cells and tissues. Proc Natl Acad Sci USA. 2024;121(2). https://doi.org/10.1073/pnas.2309125121
71. Lou SS, Kennard AS, Koslover EF, Gutierrez E, Groisman A, Theriot JA. Elastic wrinkling of keratocyte lamellipodia driven by myosin-induced contractile stress. Biophys J. 2021;120(9):1578–91. https://doi.org/10.1016/j.bpj.2021.02.022 PMID: 33631203
72. Clift R, Grace J, Weber M. Bubbles, Drops, and Particles. 1978. https://doi.org/10.1016/C2013-0-06100-3
73. Underhill PT, Doyle PS. On the coarse-graining of polymers into bead-spring chains. J Non-Newtonian Fluid Mech. 2004;122(1–3):3–31. https://doi.org/10.1016/j.jnnfm.2003.10.006
74. Kim T, Hwang W, Lee H, Kamm RD. Computational analysis of viscoelastic properties of crosslinked actin networks. PLoS Comput Biol. 2009;5(7):e1000439. https://doi.org/10.1371/journal.pcbi.1000439 PMID: 19609348
75. Dürre K, Keber FC, Bleicher P, Brauns F, Cyron CJ, Faix J, et al. Capping protein-controlled actin polymerization shapes lipid membranes. Nat Commun. 2018;9(1):1630. https://doi.org/10.1038/s41467-018-03918-1 PMID: 29691404
76. Bell GI. Models for the specific adhesion of cells to cells. Science. 1978;200(4342):618–27. https://doi.org/10.1126/science.347575 PMID: 347575
77. Jung W, Murrell MP, Kim T. F-actin cross-linking enhances the stability of force generation in disordered actomyosin networks. Comp Part Mech. 2015;2(4):317–27. https://doi.org/10.1007/s40571-015-0052-9
78. Kim T. Determinants of contractile forces generated in disorganized actomyosin bundles. Biomech Model Mechanobiol. 2014;14(2):345–55. https://doi.org/10.1007/s10237-014-0608-2
79. Muresan CG, Sun ZG, Yadav V, Tabatabai AP, Lanier L, Kim JH, et al. F-actin architecture determines constraints on myosin thick filament motion. Nat Commun. 2022;13(1):7008. https://doi.org/10.1038/s41467-022-34715-6 PMID: 36385016